Ore Geology Reviews 149 (2022) 105058

Contents lists available at ScienceDirect

Ore Geology Reviews

journal homepage: www.elsevier.com/locate/oregeorev

Lithium mineralization during evolution of a magmatic–hydrothermal system: Mineralogical evidence from Li-mineralized pegmatites in Altai, NW China

Jian-Zheng Chen [a,b], Hui Zhang [a,*], Yong Tang [a], Zheng-Hang Lv [a], Yi An [a,b], Meng-Tao Wang [a,b], Kun Liu [a,b], Yu-Sheng Xu [a,b]

[a] Key Laboratory of High-temperature and High-pressure Study of the Earth's Interior, Institute of Geochemistry, Chinese Academy Sciences, Guiyang 550081, China
[b] College of Earth and Planetary Science, University of Chinese Academy of Sciences, Beijing 100049, China

ARTICLE INFO

Keywords:
Pegmatite
Li mineralization
Li-rich minerals
Magmatic–hydrothermal evolution
Altai

ABSTRACT

Pegmatite lithium (Li) deposits are usually associated with high fractionation and complex evolution of the magmatic–hydrothermal system. However, the mechanism that accounts for the evolution of the magmatic–hydrothermal system and Li mineralization remains unclear. The Li-mineralized pegmatites in the Altai orogenic belt in northwest of China, including the Koktokay No.3 pegmatite, Xiaohusite No.91 pegmatite, and Talati No.1 pegmatite used in this study, show different rock-formation ages and ore deposit scales but similar magmatic–hydrothermal evolution and ore mineral assemblage. This study focuses on the relative contributions of magmatic and hydrothermal processes to the formation of Li deposits. Therefore, the texture and compositions of Li-rich minerals (micas, spodumene, montebrasite, and holmquistite) were systematically analyzed in these three pegmatites. From the outer to the inner zones of the studied pegmatites, micas varied from muscovite to Li-bearing muscovite and Li-bearing phengite to zinnwaldite to lepidolite, with decreasing K/Rb ratios (27.4–5.3, 27.0–4.1, and 15.5–5.0, respectively, in Koktokay No.3 pegmatite, Xiaohusite No.91 pegmatite and Talati No.1 pegmatite) and increasing Li (545–12540, 652–35519, and 627–2599 ppm), Rb (3388–16820, 3447–20970, and 5930–17096 ppm), Cs, Ta, and F concentrations, showing that fractional crystallization is the most important factor controlling Li mineralization in the magmatic stage. However, primary muscovite, spodumene, and montebrasite were altered by subsequent hydrothermal fluids, forming F, Li-rich mica rims, secondary montebrasite, secondary spodumene, and other secondary minerals. The occurrence of holmquistite indicated that Li-rich hydrothermal fluids entered into wall rock. These processes indicate that Li reactivation and migration during the hydrothermal stage would destroy Li mineralization in the pegmatite.

1. Introduction

Lithium (Li) is becoming increasingly crucial as a strategic metallic element in many applications, such as aerospace, lithium-ion batteries, and low-carbon energy (Sovacool et al., 2020; Xu et al., 2021). Spodumene-bearing pegmatites, regarded as an important type of Li deposit, commonly occur complex magmatic–hydrothermal evolution in high degrees of fractional crystallization of silicate melts (Kaeter et al., 2018; Linnen and Cuney, 2005; Linnen and Cuney, 2005; Liu et al., 2020; Yin et al., 2020). The relationship between magmatic–hydrothermal evolution and Li mineralization is crucial for understanding the metallogenic mechanism of Li-mineralized pegmatites. Therefore, one of the challenges is to estimate the relative contributions of the magmatic and hydrothermal processes to Li mineralization. To date, the metallogenic mechanism of rare-metal elements proposed for the granite–pegmatite system mainly includes fractional crystallization (Hulsbosch et al., 2014; Shearer et al., 1992; Wu et al., 2017), magmatic immiscibility (Veksler and Thomas, 2002; Webster et al., 1997), supercritical melt/fluid (Thomas and Davidson, 2016; Thomas et al., 2019), and constitutional zone refining (London, 2018).

The textures and chemical compositions of ore-bearing oxide minerals, rock-forming minerals, and even accessory minerals are commonly used to trace the magmatic–hydrothermal processes that take place in granitic pegmatites and related rare-metal mineralization (Li

* Corresponding author.
E-mail address: zhanghui@mail.gyig.ac.cn (H. Zhang).

https://doi.org/10.1016/j.oregeorev.2022.105058
Received 26 March 2022; Received in revised form 28 July 2022; Accepted 30 July 2022
Available online 4 August 2022

et al., 2021a; Lichtervelde et al., 2008; Roda et al., 2007). Most previous studies on mineralogy mainly focused on the magmatic–hydrothermal processes in pegmatite deposits. For example, the Koktokay No.3 pegmatite, being one of the most famous super-large, rare-metal deposits in the world, has been extensively studied in terms of its mineralogical characteristics, with a focus on micas and feldspars (Zhou et al., 2013), tourmaline (Wu et al., 2015; Zhang et al., 2004a; Zhang et al., 2008a; Zhang et al., 2008b),apatite (Bai et al., 2021; Liu and Zhang, 2005), zircon (Zhang et al., 2004b), columbite-group minerals (Messing et al., 1992; Zhang et al., 2004b), quart (Tang and Zhang, 2018), and garnet and beryl (Wang et al., 2009; Zhou et al., 2015). Some mineralogical studies on the Xiaohusite No.91 pegmatite have been recently conducted (Tian et al., 2021; Xu et al., 2019). Few mineralogical studies have focused on the Talati No.1 pegmatite. In addition, the mineralization scale and mineral textural zoning complexity of these three pegmatite are different, these three pegmatites are chosen as the representative Li deposits for this study. Specifically, there are few targeted studies on the relative contributions of the magmatic and hydrothermal processes to the Li mineralization of the pegmatites. Therefore, it is necessary to explore the metallogenic mechanism of Li by conducting a comparative study on mineralogy between these Li-mineralized pegmatites in Altai, NW, China.

This study presents the results of major- and trace-element analyses of Li-bearing minerals (micas, spodumene, montebrasite, and holmquistite) between the three Li-mineralized pegmatites. By comparing similarities and differences, the study aims to elucidate the relationships between the Li mineralization and the magmatic–hydrothermal evolution of highly fractionated granitic melts and reveal the relative contributions of magmatic and hydrothermal processes to the formation of Li deposits. The results show that magma fractional crystallization plays a critical role in Li mineralization during the magmatic stage. Furthermore, reactivation and migration of Li during the hydrothermal stage would destroy Li mineralization.

2. Geological background

2.1. Regional geology

The Chinese Altai, regarded as a key portion of the Central Asian Orogenic Belt, is located in northwest China and is laid at the junction of Kazakstan, Russia, and Mongolia, (Fig. 1a). The formation of the Chinese Altai has been considered as the magmatic arc formed by multiple subduction–accretion processes occurring at an active continental margin during the Middle Cambrian to Early Permian (Cai et al., 2011a; Cai et al., 2011b; Cai et al., 2012; Cai et al., 2010, 2011c; Jiang et al., 2011; Sun et al., 2009). Separated by the Hongshanzui–Nuoerte Fault, Abagong–Kuerti Fault, Fuyun–Xibodu Fault, and Erqis Fault, the Chinese Altai consists of four major tectonic domains from the north to south: the North Altai, Central Altai, Qiongkuer, and Erqis domains based on its stratigraphy, metamorphism, deformation pattern, and magmatic activity (Fig. 1b) (Cai et al., 2011a; Cai et al., 2011c; Long et al., 2008; Yuan et al., 2007).

As shown in Fig. 1b, the North Altai domain (unit I) is made up of metavolcanic and metasedimentary rocks dating from the Devonian to

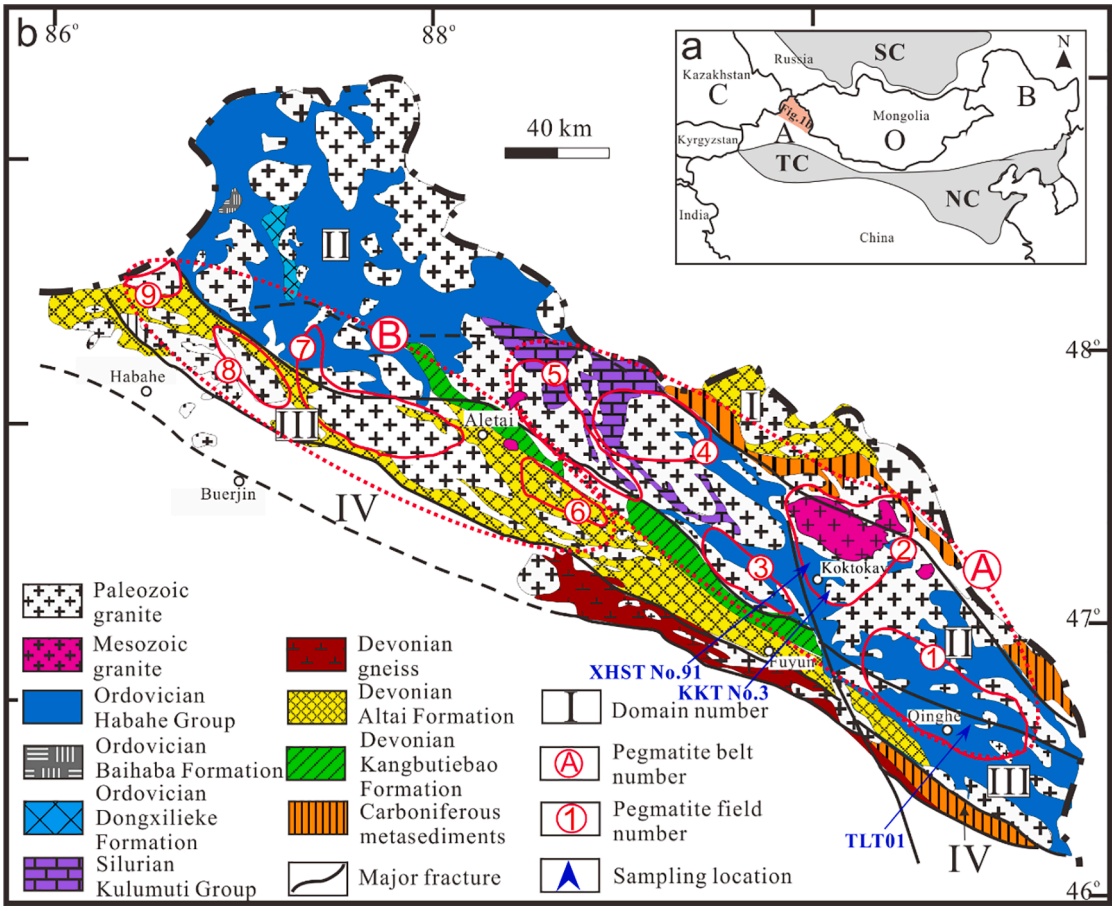

Fig. 1. Tectonic location (a) and geological sketch map of the Chinese Altai (b) modified from (Lv et al., 2018; Windley et al., 2002). Abbreviation: CAOB = Central Asian Orogenic Belt; SC = Siberia Craton; TC = TarimCraton; NC = North China Craton. Code: I, North Altai domain; II, Central Altai Domain; III, Qiongkuer domain; IV, Erqis domain. A, Halong-Qinghe pegmatite sub-belt; B, Jiamanhaba-Xiaokalasu pegmatite sub-belt. 1, Qinghe pegmatite field; 2, Koktokay pegmatite field; 3, Kuwei-Jiebiete pegmatite field; 4, Kelumute-Jideke pegmatite field; 5, Kalaeerqisi pegmatite field; 6, Dakalasu-Kekexier pegmatite field; 7, Xiaokalasu-Qiebielin pegmatite field; 8, Hailiutan-Yeliuman pegmatite field; 9, Jiamanhaba pegmatite field.

Carboniferous periods. The Central Altai domain (unit II) is a large domain that is composed of a thick turbidite and pyroclastic sequence of the Habahe Group, volcanic molasse dating from the upper Ordovician, terrigenous clastic sequences of the Dongxilieke and Baihaba Formations, and metasandstone of the Kulumuti Formation dating from the middle–upper Silurian. The Qiongkuer domain (unit III) consists of Paleozoic clastic and volcanic rocks, which are subdivided into the early Devonian Kangbutiebao Formation and the Middle Devonian Altai Formation, respectively. The Erqis domain (unit IV) is largely covered by Quaternary sediments in the western part, while the southestern part is composed of Devonian fossiliferous successions of the Kangbutiebao Formation that are in turn overlain by Late Carboniferous formations (BGMRX (Bureau of Geology and Mineral Resources of Xinjiang Uygur Autonomous Region), 1993; Windley et al., 2002).

2.2. Geology of pegmatite fields and the studied pegmatites

Based on the previously reported statistics, approximately 100,000 pegmatite dykes were mainly exposed in the two pegmatite sub-belts of the Chinese Altai (Wu and Zou, 1989). The Halong–Qinghe pegmatite sub-belt is located in the Central Altai domains (A in Fig. 1b) and consists of five pegmatite fields: Qinghe, Koktokay, Kuwei–Jiebiete, Kelumute–Jideke, and Kalaeerqisi (1–5 in Fig. 1b, respectively). The Jiamanhaba–Dakalasu pegmatite sub-belt is located in the Qiongkuer domain (B in Fig. 1b) and consists of four pegmatite fields: Dakalasu–Kekexier, Xiaokalasu–Qiebielin, Hailiutan–Yeliuman, and Jiamanhaba (6–9 in Fig. 1b, respectively) (Wu and Zou, 1989; Zou and Li, 2006).

2.2.1. Koktokay No.3 pegmatite

The Koktokay No.3 pegmatite (KKT No.3) is located in the southwestern of the Koktokay pegmatite field. Its geographical coordinates are N47°12′24″, E89°48′54″. The pegmatite is composed of an oval "cupola" part and a gently dipping vein at the bottom (Fig. 2a). The cupola-shaped part is 250 × 250 × 250 m in length, width, and depth, respectively, with a strike of NW 335°, NE inclination, and dip angle of 75°–90°, showing a typical concentric ring structure of nine textural zones from the rim to the core: I. graphic pegmatite zone; II. saccharoidal albite zone; III. blocky microcline zone; IV. muscovite–quartz zone; V. cleavelandite–spodumene zone; VI. quartz–spodumene zone; VII. lamellar albite–muscovite zone; VIII. lepidolite–lamellar albite zone; and IX. blocky quartz and microcline core (Zhu et al., 2000; Zou and Li, 2006). Zone I is characterized by a typical microcline and quartz graphic texture with minor euhedral muscovite. Zone II consists of dominant white and fine-grained albite. Coarse-grained beryl closely coexists with apatite in this zone. Zone III mainly hosts large (~30 cm) microcline crystals. Zone IV is mainly composed of large-grained and euhedral muscovite and quartz. Zone V is mainly composed of platy albite, pink spodumene, and quartz (Fig. 2d). Albite crystals grow radially, closely coexisting with pink spodumene. Zone VI is mainly

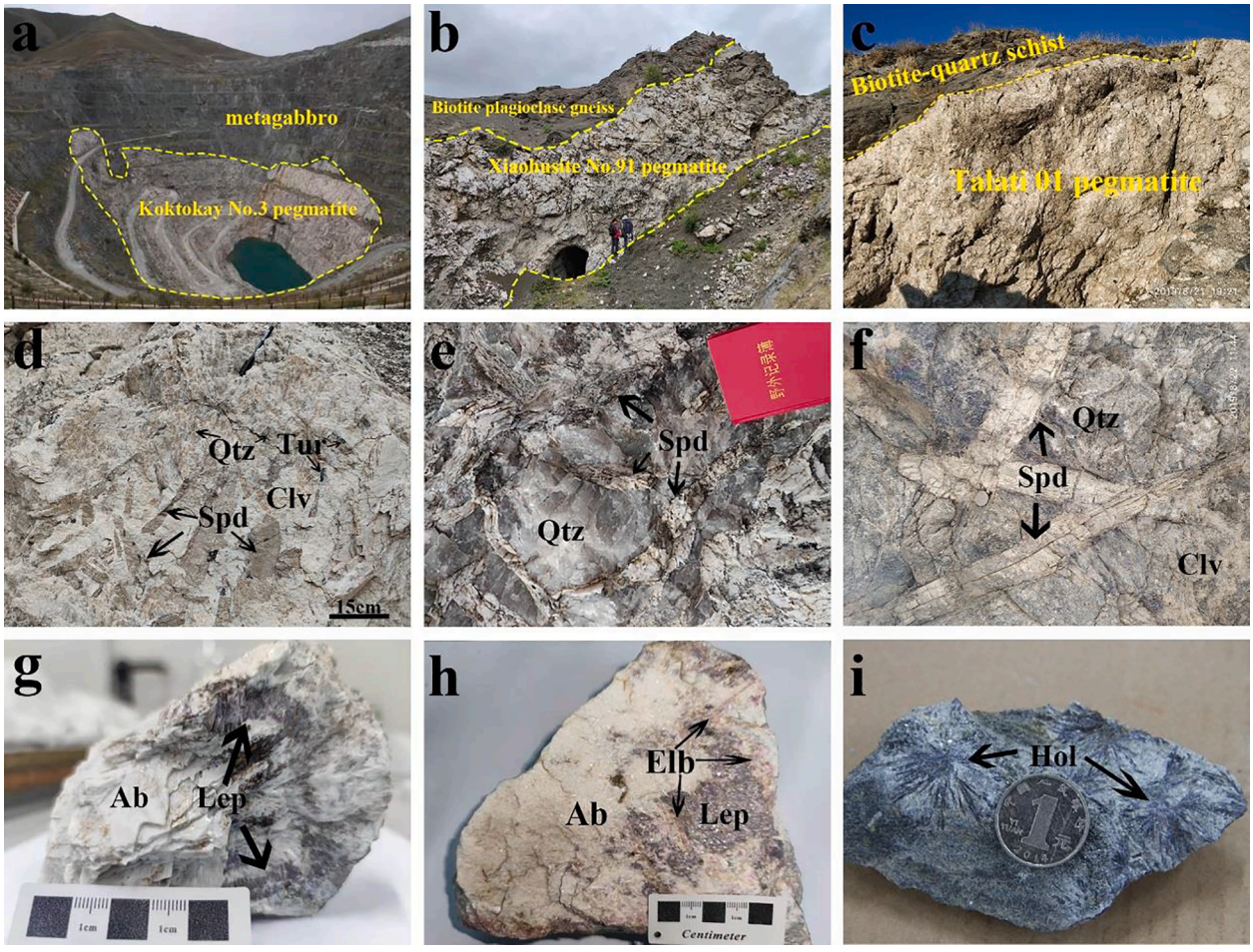

Fig. 2. Field photographs of the KKT No.3 pegmatite (a), XHST No.91 pegmatite (b), TLT No.1 pegmatite (c). (d, g) hand-specimen showing the cleavelandite-spodumene zone (V) and lepidolite-lamellar albite zone (VIII) of the KKT No.3 pegmatite. (e, h) hand-specimen showing quartz-spodumene core zone (VI) and elbaite-lepidolite association of the XHST No.91 pegmatite. (f, i) hand-specimen showing quartz-cleavelandite-spodumene zone (V) and holmoustitization in the host rocks of the TLT No.1 pegmatite. Abbreviations: Clv = cleavelandite; Ab = albite; Lep = lepidolite; Qtz = quartz; Spd = spodumene; Tur = tourmaline; Elb = elbaite; Hol = holmquistites.

composed of quartz and pink spodumene. Zone VII is mainly composed of lamellar albite and muscovite. In zone VIII, lilac fine- to medium-grained lepidolite occurs in a pod shape with large-grained lamellar albite (Fig. 2g). Zone IX consists of dominant quartz and microcline. Few samples are collected in this zone now owing to previous mining operations. Zones I–IV were named as the outer pegmatite zones, which account for 70 % of the zone volume. Zones V–IX were named as the inner pegmatite zones, where Li mineralization mainly occurs (Zhang et al., 2004b). Being a super-large ore deposit containing Li, Be, Nb, Ta, Rb, Cs, and Hf, the KKT No. 3 pegmatite is emplaced in the metagabbro pluton (Zou and Li, 2006). Chen (2011) analyzed the age of the KKT No.3 pegmatite (215–212 Ma) using the U–Pb zircon method based on laser ablation inductively coupled-plasma mass spectrometry (LA-ICPMS), which is approximately highly consistent with the results obtained from the U–Pb zircon (220 ± 9 Ma) (Wang et al., 2007), U–Pb columbite–tantalite (218 ± 2 Ma) (Che et al., 2015), and Re–Os molybdenite (210–208 Ma) (Liu et al., 2014) methods.

2.2.2. Xiaohusite No.91 pegmatite

The Xiaohusite No.91 pegmatite (XHST No.91) is a medium ore deposit containing Li, Be, Ta, Nb, which is located in the middle right bank of the Kexiekusite river, and belongs to the Koktokay pegmatite field. Its geographical coordinates are N47°17′07.70″, E89°46′32.86″. The pegmatite has a length of 400 m and width up to 133 m, with irregular branching and bending shape (Fig. 2b). The general strike of the main vein is NE 75°–80°, NW inclination. The XHST No.91 pegmatite occurs as an intrusion in the biotite plagioclase gneiss, having a sharp contact and unidirectional solidification texture (UST: the elongate growth of crystals inward from contact with the host rock) (Fig. 2b). Similar to the mineral assemblage textural zones of the KKT No.3 pegmatite, the following five textural zones from the rim to the core have been identified in the XHST No.91 pegmatite: I. graphic pegmatite zone, III. blocky microcline zone, IV. Muscovite–quartz zone, V. (quartz)–cleavelandite–spodumene zone, VI. quartz–spodumene zone. II. The saccharoidal albite zone is missing. Zone I is composed mainly of microcline and quartz with graphic texture. Zone III consists mainly of large microcline, minor quartz, muscovite, and shorl. Zone IV mainly contains quartz, muscovite, and variable amounts of shorl. Zone V contains mainly quartz, platy albite, and pink spodumene. Zone VI is characterized by irregular pink spodumene and quartz (Fig. 2e). Some pink elbaite grains are closely associated with lepidolite (Fig. 2h). Zones I, III, and IV were named as the outer pegmatite, whereas Zones V and VI were named as the inner pegmatite. Ren et al. (2011) dated the pegmatite at 190.6 ± 1.2 Ma using the LA-ICPMS U–Pb zircon method.

2.2.3. Talati No.1 pegmatite

The Talati No.1 pegmatite (TLT No.1) is a small ore deposit containing Li, Be, Ta, and Nb and is located in the midportion of the Qinghe pegmatite field. Its geographical coordinates are N46°42′50″, E90°32′38″. The TLT No.1 pegmatite is sharply intruded into the biotite–quartz schist (Fig. 2c), where a large amount of holmquistite in the exocontact zone is found and unidirectional solidification texture inward from contact with the host rock (Fig. 2i). The outcrop has a length of 105 m and width of 4–8 m, with a strike of WNW 310° and dip angle of 80°. According to the mineral assemblage textural zones of the KKT No.3 pegmatite, TLT No.1 pegmatite is divided into four textural zones: II. the saccharoidal albite zone, III. the blocky microcline zone, IV. the quartz–muscovite zone, V. the quartz–cleavelandite–spodumene zone. The graphic pegmatite zone (zone I) is missing. Zone II is the outermost zone that is in sharp contact with the host rock and contains mainly fine-grain and white albite, along with euhedral green crystals of beryl. Zone III locally occurs as large microcline and minor muscovite and quartz. Zone IV mainly comprises large-grained euhedral muscovite and quartz. Zone V contains mainly quartz, platy albite, and spodumene megacrysts of several to tens of centimeters length (Fig. 2f). Zones II, III, and IV were named as the outer pegmatite, while zone V was named as the inner pegmatite. Using the LA-ICPMS U–Pb zircon method, Lv et al. (2018) dated this pegmatite 385.9 ± 3.5 Ma.

3. Samples and analytical methods

Samples were collected from the different textural zones from open pits in the Koktokay No.3 pegmatite, Xiaohusite No.91 pegmatite and Talati No.1 pegmatite. The mica samples were selected from the different textural zones of the studied pegmatites. The spodumene and montebrasite samples selected for major-element analysis were derived mainly from the inner zones of the pegmatites. However, the holmquistite sample was collected only from the host rock of the Talati No.1 pegmatite. All these samples were prepared in thin sections (50–70 μm thickness) for petrographic observations and quantitative element analysis. Moreover, the analyses of mica, spodumene, and montebrasite were performed in the same thin section when these occurred together. The detailed analytical procedures are as follows.

3.1. Scanning electron microscopy (SEM) and energy dispersive spectrometry (EDS)

Preliminary petrographic observations were made using an optical microscope. Mineral identification and back-scattered electron (BSE) images were obtained using a FEI Scios SEM equipped with an EDS at the center for lunar and planetary sciences, Institute of Geochemistry Chinese Academy of Sciences. Operating conditions of 20-kV acceleration voltage, 0.8-nA beam current, and a working distance of 7 mm were adopted for all EDS analyses.

3.2. Determination of major elements using electron probe micro-analyzer (EPMA)

The major elements in micas, spodumene, montebrasite, and holmquistite were determined using a JEOL JXA-8230 EPMA at the State Key Laboratory of Ore Deposit Geochemistry at the Institute of Geochemistry Chinese Academy of Sciences. Operating conditions of 25 kV, 10nA, and a 10-μm beam were adopted for minerals analyses. Peak and background counting times were 10 and 5 s, respectively. The results were reduced using a ZAF correction routine. For mica, the standard samples were biotite (K, Ti, Mg, and Fe), plagioclase (Na and Si), apatite (P and F), topaz (Al), pyrope (Mn and Ca), benitoite (Ba), and tugtupite (Cl). For spodumene, the standard samples were chrome diopside (Ca, Cr, Mg, and Fe), orthoclase (Si and K), pyrope (Ti and Mn), plagioclase (Na and Al), and apatite (P). For montebrasite and holmquistites, the standard samples were apatite (Ca, Na, Sr, F, and P), pyrope (Mg, Mn, and Fe), tugtupite (Cl), celestite (S), and topaz (Al). The results for micas, spodumene, and montebrasite are shown in Supplementary Tables 1, 2, and 3, respectively, and the result for holmquisite is shown in Table 5.

3.3. Analysis of trace elements using LA-ICPMS

In situ trace-element analyses of micas and holmquistite were performed using a LA-ICPMS at the State Key Laboratory of Ore Deposit Geochemistry at the Institute of Geochemistry Chinese Academy of Sciences. An Agilent 7700X ICP-MS instrument was coupled to a RESOlution S-155 193-nm laser ablation system. Single-spot ablation was adopted with a laser beam of 40 μm. The laser energy measured 85 mJ, and the ablation frequency was 7 Hz. Helium was used as a carrier gas, and nitrogen was used to enhance sensitivity. Prior to analysis, the LA-ICPMS system was optimized using NIST SRM 610 glass to achieve the maximum signal intensity and low oxide rates. Multiple glass reference materials (BCR-2G, BHVO-2G, BIR-1G, and KL2-G) were used as a reference for external calibration. The method of multiple external standards and no internal standard was used for quantitative calculations of the element concentrations. The normalized element was Si. Offline processing of analytical data (including sample and blank signal

selection, instrument sensitivity drift correction, and element content calculation) was conducted using the ICPMSDataCal software to finish (Liu et al., 2008). The full dataset of muscovite is listed in Supplementary Table 4 and that of holmquisite is listed in Table 5. The measured trace-element concentrations of NIST SRM 610, BCR-2G, BHVO-2G, BIR-1G, and KL2-G glasses and their recommended values are listed in Supplementary Table 5.

4. Results

4.1. Texture and compositional characteristics of micas

Muscovite has similar homogeneous textures in the outer zones of the studied pegmatites. It commonly occurs in its primary phase. Some muscovite flakes display complex core–rim zoning with chemical heterogeneity and show bright and dark domains in BSE images (Fig. 3a, b, d). However, the inner zone of the TLT No.1 pegmatite mainly hosts primary muscovite, which generally appears as large flakes with curved cleavages, and vimineous apatite along the cleavage planes (Fig. 3e, f). Secondary muscovite is much smaller than primary muscovite and is commonly present in the symplectite of spodumene and quartz (Fig. 6a, c, e) or occurs along the cleavage planes of spodumene (Fig. 6f). Lepidolite occurs in its primary or secondary phase along the cleavage planes of spodumene and montebrasite. Primary lepidolite mainly occurs as euhedral grains, which are up to 2 mm in length (Fig. 3c) and are mainly distributed in zones V, VI, and VIII of the KKT No.3 pegmatite and in zones V and VI of the XHST No.91 pegmatite. There are also some minor traces in the TLT No.91 pegmatite. However, secondary lepidolite

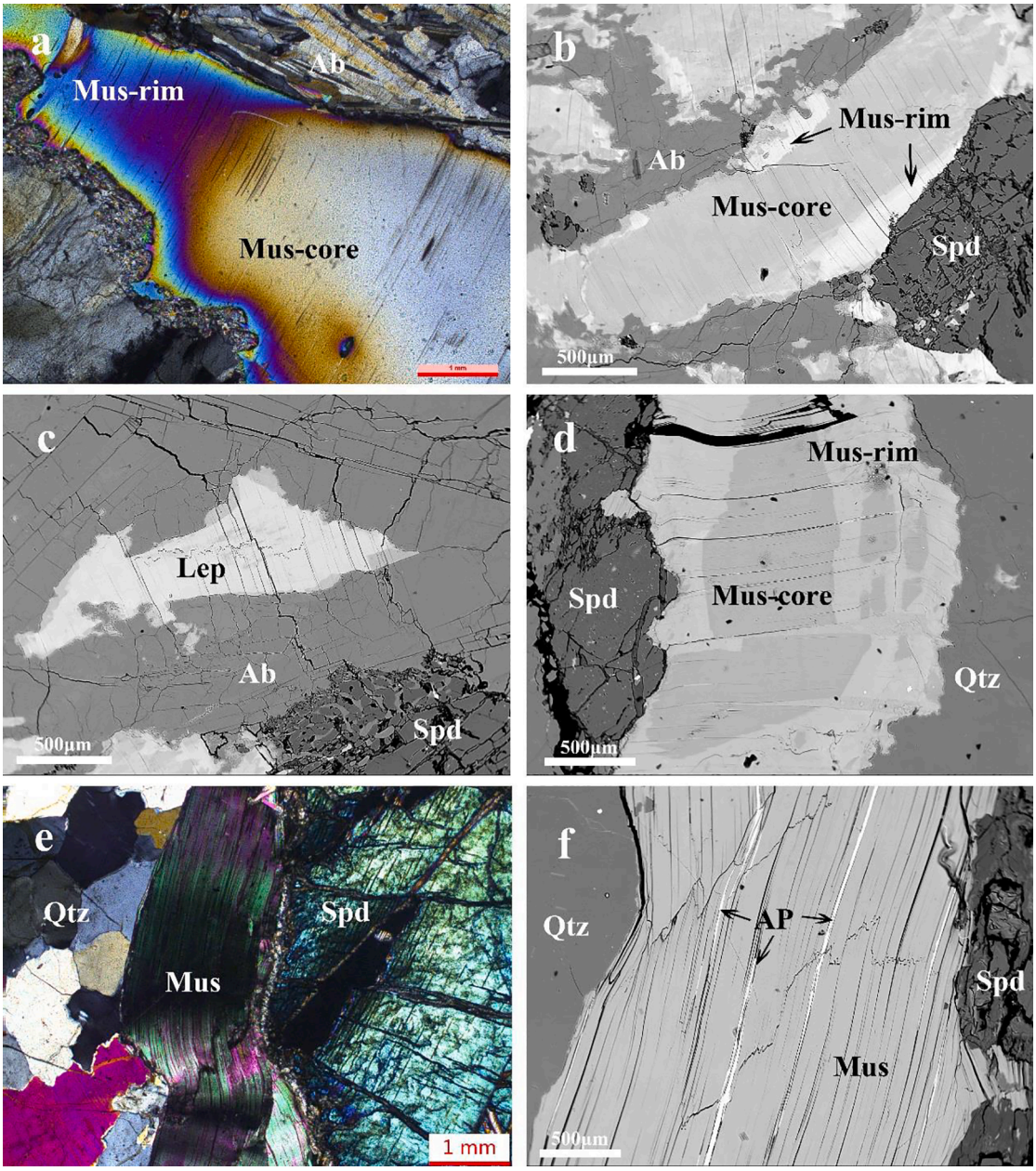

Fig. 3. Photomicrographs and backscattered electron (BSE) images of micas in the inner zone of the KKT No.3 pegmatite (a-c), XHST No.91 pegmatite (d), and TLT No.1 pegmatite (e, f). (a) Under orthogonal polarized light microscope, the core and rim of mica are obviously different, (b) BSE image of muscovite intergrown with spodumene show zoning. (c) Euhedral lepidolite intergrown with spodumene and albite. (d) Muscovite show core and rim zoning. (e) Euhedral muscovite around the rim of spodumene. (f) Apatite in cleavage planes of muscovite. Abbreviation: Ab = albite, Qtz = quartz, Mus = muscovite, Spd = spodumene, Ap = apatite, Lep = lepidolite.

occurs in spodumene and montebrasite with an irregular shape (Figs. 6b, d; 7).

In studied samples, micas show systematic chemical variability between different textural zones of pegmatites. Structural formulas for the average chemical compositions shown in Table 2 were calculated based on 24 anions (O, OH, and F). In the (Mg–Li) versus the (Fe + Mn + Ti–Al^{VI}) diagram (Fig. 4), as set up by Tischendorf et al. (1997), of the KKT No.3 pegmatite, zones I–IV mainly host muscovite; zone III hosts some amounts of Li-bearing phengite; and zones V and VI host muscovite, Li-bearing muscovite, Li-bearing phengite, and lepidolite. Zone VII mainly hosts muscovite, while zone VIII hosts muscovite, zinnwaldite, and lepidolite. In the XHST No.91 pegmatite, zones UST, I, III, and IV host mainly muscovite. Li-bearing muscovite and zinnwaldite are found in zone V, while lepidolite is mainly found in zone VI. However, muscovite is found in all textural zones of the TLT No.1 pegmatite, while primary Li-rich micas are missing.

Muscovites in the outer zones of the pegmatites are homogeneous. However, the concentrations of F and Li_2O* generally increase from zones I to IV of the KKT No.3 pegmatite; zones I, III to IV of the XHST No.91 pegmatite; and zones II, III to IV of the TLT NO.1 pegmatite (Table 2, Fig. 5). By contrast, muscovites in the inner zones of the KKT No.3 pegmatite (zones V–VIII) and XHST No.91 pegmatite (zones V and VI) exhibit compositional zoning that consists of core and rim domain (Fig. 3a, b, d), and occurrence of euhedral lepidolite (Fig. 3c, Table 2). The rim domains are brighter than the core ones in BSE images, with a sharp compositional boundary, which is consistent with the higher content of Li_2O* (1.18–4.28 wt% in the KKT No.3 pegmatite; 2.57–3.56 wt% in the XHST No.91 pegmatite), F (2.25–6.05 wt% in the KKT No.3 pegmatite; 4.12–5.26 wt% in the XHST No.91 pegmatite), and FeO (2.19–3.38 wt% in the KKT No.3 pegmatite; 1.02–1.14 wt% in the XHST No.91 pegmatite). The concentrations of F and Li_2O* gradually increase from the rim domains of muscovites in zones V, VI, and VIII in the KKT No.3 pegmatite but gradually decrease in the core domains (Table 2, Fig. 5). Muscovites in zone V of the TLT No.1 pegmatite are euhedral and homogeneous, with lower concentrations of F (0.14–2.10 wt%) and Li_2O (0.03–1.05 wt%), and apatite veinlets occur along cleavage planes (Fig. 3e, f).

Table 1
Geologic characteristic of the three Li-mineralized pegmatites in the Chinese Altai.

pegmatite	Koktokay No.3	Xiaohusite No.91	Talati No.1
Geographical coordinates	N47°12′24″ E89°48′54″	N47°17′07.70″ E89°46′32.86″	N46°40′57.40″ E90°31′12.61″
Pegmatite field	Koktokay	Koktokay	Qinghe
Host rocks	Metagabbro	Biotite plagioclase gneiss	Biotite-quartz schist
Contact relationship	Sharp	Sharp	Sharp
Shape	Oval	Branching	Vein
Length and width (m)	250 and 250	400 and 133	105 and 4–8
Strike	NW335°	NE75°	NW301°
Mineralization type	Li-Be-Nb-Ta-Rb-Cs-Hf	Li-Be-Nb-Ta	Li-Be-Nb-Ta
Scale	Super-large	middle	small
Primary Li-bearing mineral	Muscovite, lepidolite, elbaite, spodumene, lithiophilite	Muscovite, lepidolite, elbaite, spodumene, montebrasite, lithiophilite	Muscovite, spodumene, montebrasite, lithiophilite
Secondary mineral	Muscovite, quartz lepidolite, apatite, spodumene	Muscovite, quartz lepidolite, apatite, montebrasite	Muscovite, quartz, lepidolite, apatite, holmquistite, montebrasite crandallite-goyazite
Zonation	I - IX	I, III - VI	II - V
Age and reference	220 ± 9 (Wang et al., 2007)	190.6 ± 1.2 (Ren et al., 2011)	385.9 ± 3.5 (Lv et al., 2018)

The Rb concentrations from the outer to inner zones have a high and wide range (3388–16820 ppm in the KKT No.3 pegmatite; 3447–20970 ppm in XHST No.91 pegmatite; and 5930–17096 ppm in TLT No.1 pegmatite). The range of K/Rb varies from 27.4 to 5.3 in the KKT No.3 pegmatite, 27.0 to 4.1 in XHST No.91 pegmatite, and 15.5 to 5 in the TLT No.1 pegmatite. The Li concentration of micas in the KKT No.3 pegmatite (545–12540 ppm) and XHST No.91 pegmatite (652–35519 ppm) are significantly higher than the TLT No.1 pegmatite (627–2599 ppm), especially in the inner zones. The decreasing K/Rb rate versus the progressive enrichment of Li, Rb, Cs, B, and Ta (Fig. 10), whereas Be and Nb have no remarkable changes. Moreover, the concentration of B (81–457 ppm) and Ga (72–118 ppm) in muscovite in TLT No.1 pegmatite are overall lower than those in XHST No.91 pegmatite (132–732 and 133–192 ppm, respectively, excluding the lepidolite sample) and KKT No.3 pegmatite (107–1122 and 43–197 ppm, respectively). However, the Ba concentrations in muscovites in the TLT No.1 pegmatite are higher than those of the other pegamtites (Fig. 10).

Photomicrographs and BSE images of micas are shown in Fig. 3. The representative average compositions and structural formulas of mica samples are shown in Table 2. The major-element composition and the structural formulas, together with minor- and trace-element compositions of all mica samples from the studied pegmatites, are listed in the appendix, respectively.

4.2. Texture and compositional characteristics of spodumene

Spodumene, which is the most important Li-bearing mineral, commonly occurs in the inner zones of the studied pegmatites (Fig. 2d–f). Based on its morphological images, spodumene can be classified into two types in the KKT No.3 pegmatite (Fig. 6a): large crystals of primary spodumene and small crystals of secondary spodumene. Photomicrographs and BSE images show that spodumene grains are altered to fine-grained and irregular veinlets of muscovite and quartz in their interior (Fig. 6a, c, e). Moreover, lepidolite, apatite, and muscovite occur in the cleavages of spodumene (Fig. 6b, d, f).

The major-element compositions of spodumene in the studied pegmatites reveal a nearly ideal stoichiometric composition, while the small number of impurities present consists mainly of FeO (0.18–1.14 wt%), Na_2O (0.05–0.75 wt%), and MgO (0.02 %–0.15 wt%). Specifically, in the KKT No.3 pegmatite, spodumene in zone V has a higher concentration of FeO (1.06–1.48 wt%) (Table 3), whereas spodumene in zones VI and VIII has a lower concentration of FeO (0.18–0.20 wt%; 0.18–0.23 wt%, respectively). Based on the stoichiometry Si = 2 atoms calculated, the content of Li_2O in spodumene in the studied pegmatites has no significant differences, it is namely about 7.90 wt%.

4.3. Texture and compositional characteristics of montebrasite

According to its BSE images, montebrasite commonly occurs with spodumene in the inner zones of the XHST No.91 pegmatite and TLT No.1 pegmatite. In the XHST No.91 pegmatite, montebrasite is altered as spongy crystal with lepidolite and apatite, forming veinlets along the cleavages between spodumene (Fig. 7a). Subhedral montebrasite, along with lepidolite and quartz, is found in the XHST No.91 pegmatitite (Fig. 7b). In the TLT No.1 pegmatite, massive montebrasite closely associated with residual spodumene, along with crandallite–goyazite series and lepidolite appear (Fig. 7c, d).

Montebrasite has a higher concentration of H_2O (5.18–5.51 wt% in the TLT No.1 pegmatite; 5.43–5.64 wt% in the XHST No.91 pegmatite) than F (1.27–2.08 wt% in the TLT No.1 pegmatite; 0.96–1.49 wt% in the XHST No.91 pegmatite). The concentrations of FeO and F in the TLT No.1 pegmatite are higher than those in the XHST No.91 pegmatite (Table 4). Intriguingly, the spongy crystal (S–Mtb in Fig. 7a) is not a standard montebrasite or augelite ($Al_2PO_4(OH)_3$) based on EPMA data (Table 4) but is regarded as a transitional product from montebrasite to augelite without Li content. Based on stoichiometry P = 1 atom

Table 2
Representative average compositions and structural formulae of micas in different textural zones in the Kokotokay No.3, Xiaohusite No.91 and Talati No.1 pegmatites.

Peg.	Kokotokay No.3												
Zone	I	II	III	IV	V		VI			VII	VIII		
N	5	10	11	8	5	4	4	6	5	6	6	6	6
Mineral	Mus				Core	Rim	Lep	Core	Rim	Mus	Lep	Core	Rim
SiO_2	45.43	46.46	48.13	46.25	49.14	49.07	51.40	47.02	49.87	46.60	52.47	46.13	53.65
TiO_2	/	/	/	0.06	0.02	0.05	/	/	/	0.01	/	0.02	/
Al_2O_3	38.38	33.12	31.22	34.35	31.15	29.66	22.60	35.27	28.40	35.31	24.58	38.45	24.51
FeO	0.80	3.97	3.26	3.73	2.79	2.99	4.25	1.28	2.91	2.44	0.50	0.23	0.49
MnO	0.02	0.23	0.15	0.23	0.66	0.75	/	0.26	/	0.37	/	0.17	/
MgO	/	0.63	0.06	0.06	/	/	1.12	/	1.06	0.05	1.17	/	1.10
CaO	/	/	/	/	/	/	/	/	/	/	/	/	/
Na_2O	0.43	0.33	0.21	0.54	0.32	0.32	0.13	0.50	0.31	0.38	0.24	0.57	0.18
K_2O	10.81	10.67	10.78	10.35	10.36	9.62	10.27	10.41	10.18	10.54	10.20	10.46	10.35
BaO	0.01	0.03	/	/	0.04	/	/	/	/	0.03	/	/	/
F	/	0.60	2.40	0.96	2.34	2.79	5.27	0.91	3.73	0.59	6.12	0.42	5.98
Li_2O*	0.00	0.20	1.26	0.37	1.22	1.53	5.20	0.34	2.26	0.19	5.51	0.12	4.21
H_2O*	4.54	4.17	3.33	4.03	3.40	3.13	2.00	4.08	2.74	4.23	1.69	4.38	1.74
O = F	/	0.25	1.01	0.40	0.99	1.18	2.22	0.38	1.57	0.25	2.58	0.18	2.52
Total	100.42	100.16	99.79	100.53	100.47	98.75	100.04	99.70	99.87	100.50	99.89	100.79	99.70
	Structural formula on the basis of 24 (O, OH, F) atoms												
Si	6.00	6.26	6.46	6.18	6.53	6.61	6.85	6.25	6.64	6.19	6.86	6.04	7.03
Al_{iv}	2.00	1.74	1.54	1.82	1.47	1.39	1.15	1.75	1.36	1.81	1.14	1.96	0.97
Al_{vi}	3.96	3.52	3.39	3.59	3.40	3.32	2.40	3.78	3.09	3.72	2.64	3.97	2.81
Ti	0.00	0.00	0.00	0.01	0.00	0.01	0.00	0.00	0.00	0.00	0.00	0.00	0.00
Fe	0.09	0.45	0.37	0.42	0.31	0.34	0.47	0.14	0.32	0.27	0.05	0.03	0.05
Mn	0.00	0.03	0.02	0.03	0.07	0.09	0.00	0.03	0.00	0.04	0.00	0.02	0.00
Mg	0.00	0.13	0.01	0.01	0.00	0.00	0.22	0.00	0.21	0.01	0.23	0.00	0.22
Li*	0.00	0.06	0.68	0.20	0.65	0.83	2.79	0.18	1.21	0.10	2.89	0.07	2.22
Ca	0.00	0.00	0.00	0.00	0.00	0.00	0.00	0.00	0.00	0.00	0.00	0.00	0.00
Na	0.11	0.09	0.06	0.14	0.08	0.08	0.03	0.13	0.08	0.10	0.06	0.15	0.04
K	1.82	1.83	1.84	1.77	1.75	1.65	1.75	1.77	1.73	1.79	1.70	1.75	1.73
Ba	0.00	0.00	0.00	0.00	0.00	0.00	0.00	0.00	0.00	0.00	0.00	0.00	0.00
OH*	4.00	3.74	2.98	3.60	3.02	2.81	1.78	3.62	2.43	3.75	1.47	3.82	1.52
F	0.00	0.25	1.02	0.40	0.98	1.19	2.22	0.38	1.57	0.25	2.53	0.17	2.48
Total	17.98	18.10	18.36	18.16	18.28	18.31	19.66	18.03	18.64	18.04	19.58	17.97	19.08
Y total	4.06	4.18	4.47	4.25	4.44	4.58	5.88	4.13	4.83	4.15	5.82	4.08	5.30
X total	1.93	1.92	1.90	1.91	1.84	1.74	1.78	1.89	1.81	1.89	1.76	1.89	1.77

Peg.	Xiaohusite No.91								Talati No.1				
Zone	UST	I	III	IV	V		VI		UST	II	III	IV	V
N	6	5	6	14	6	6	14	6	3	6	11	6	20
Mineral	Mus				Core	Rim	Lep	Mus	Mus				
SiO_2	45.87	45.09	46.57	46.53	46.31	53.61	53.81	45.64	45.80	46.44	46.85	45.64	46.02
TiO_2	0.09	0.02	0.08	0.10	0.04	/	/	0.02	0.03	0.44	0.37	0.49	0.15
Al_2O_3	36.22	37.93	34.20	33.71	37.54	28.07	22.31	37.29	35.88	33.39	33.71	32.79	34.66
FeO	1.61	1.35	2.38	2.79	0.93	1.02	2.46	0.70	2.16	2.50	2.65	2.92	1.93
MnO	0.11	0.02	0.15	0.09	0.11	0.33	0.27	0.10	0.03	0.03	0.05	0.02	0.03
MgO	0.33	/	0.87	0.75	0.15	/	/	0.09	0.62	1.16	1.19	1.12	0.77
CaO	/	/	/	/	/	/	0.04	/	/	/	/	/	/
Na_2O	0.62	0.61	0.57	0.45	0.71	0.12	0.23	0.63	0.98	0.41	0.45	0.43	0.42
K_2O	10.61	10.56	10.63	10.73	10.26	10.48	10.58	10.39	9.76	10.70	10.18	10.73	10.61
BaO	0.03	/	/	/	/	0.03	/	/	/	0.05	0.03	/	/
F	0.19	/	0.48	1.04	0.19	4.12	4.59	0.45	0.05	0.69	0.67	0.83	0.42
Li_2O*	0.04	0.00	0.15	0.41	0.04	2.57	5.89	0.14	0.01	0.24	0.23	0.31	0.12
H_2O*	4.41	4.52	4.26	3.99	4.48	2.68	2.41	4.30	4.47	4.15	4.19	4.02	4.26
O=F	0.08	/	0.20	0.44	0.08	1.73	1.93	0.19	0.02	0.29	0.28	0.35	0.18
Total	100.04	100.10	100.13	100.17	100.67	101.29	100.66	99.54	99.77	99.89	100.28	98.95	99.22
	Structural formula on the basis of 24 (O, OH, F) atoms												
Si	6.10	5.98	6.22	6.22	6.08	6.94	7.04	6.07	6.11	6.23	6.24	6.20	6.18
Al_{iv}	1.90	2.02	1.78	1.78	1.92	1.06	0.96	1.93	1.89	1.77	1.76	1.80	1.82
Al_{vi}	3.79	3.92	3.60	3.54	3.90	3.22	2.48	3.91	3.74	3.50	3.52	3.45	3.67
Ti	0.01	0.00	0.01	0.01	0.00	0.00	0.00	0.00	0.00	0.04	0.04	0.05	0.02
Fe	0.18	0.15	0.27	0.31	0.10	0.11	0.27	0.08	0.24	0.28	0.29	0.33	0.22
Mn	0.01	0.00	0.02	0.01	0.01	0.04	0.03	0.01	0.00	0.00	0.01	0.00	0.00
Mg	0.06	0.00	0.17	0.15	0.03	0.00	0.00	0.02	0.12	0.23	0.24	0.23	0.15
Li*	0.02	0.00	0.08	0.22	0.02	1.34	3.10	0.07	0.00	0.13	0.12	0.17	0.07
Ca	0.00	0.00	0.00	0.00	0.00	0.00	0.01	0.00	0.00	0.00	0.00	0.00	0.00
Na	0.16	0.16	0.15	0.12	0.18	0.03	0.06	0.16	0.25	0.11	0.12	0.11	0.11
K	1.80	1.79	1.81	1.83	1.72	1.73	1.77	1.76	1.66	1.83	1.73	1.86	1.82
Ba	0.00	0.00	0.00	0.00	0.00	0.00	0.00	0.00	0.00	0.00	0.00	0.00	0.00

(*continued on next page*)

Table 2 (*continued*)

Peg.	Xiaohusite No.91								Talati No.1				
Zone	UST	I	III	IV	V		VI		UST	II	III	IV	V
N	6	5	6	14	6	6	14	6	3	6	11	6	20
Mineral	Mus				Core	Rim	Lep	Mus	Mus				
OH*	3.92	4.00	3.80	3.56	3.92	2.31	2.10	3.81	3.98	3.71	3.72	3.64	3.82
F	0.08	0.00	0.20	0.44	0.08	1.69	1.90	0.19	0.02	0.29	0.28	0.36	0.18
Total	18.04	18.02	18.10	18.19	17.97	18.47	19.70	18.01	18.03	18.13	18.07	18.20	18.05
Y total	4.07	4.07	4.14	4.25	4.07	4.71	5.88	4.09	4.12	4.19	4.22	4.23	4.13
X total	1.96	1.94	1.96	1.95	1.90	1.76	1.83	1.92	1.91	1.94	1.85	1.97	1.93

UST: unidirectional solidification texture (the elongate growth of crystals inward from a contact with host rock); n: determined points; /: below detection limit; *: oxides recalculated from EPMA data, Li_2O content of micas was calculated following (Tischendorf et al., 1997), and H_2O was calculated following (Tindle and Webb, 1990).

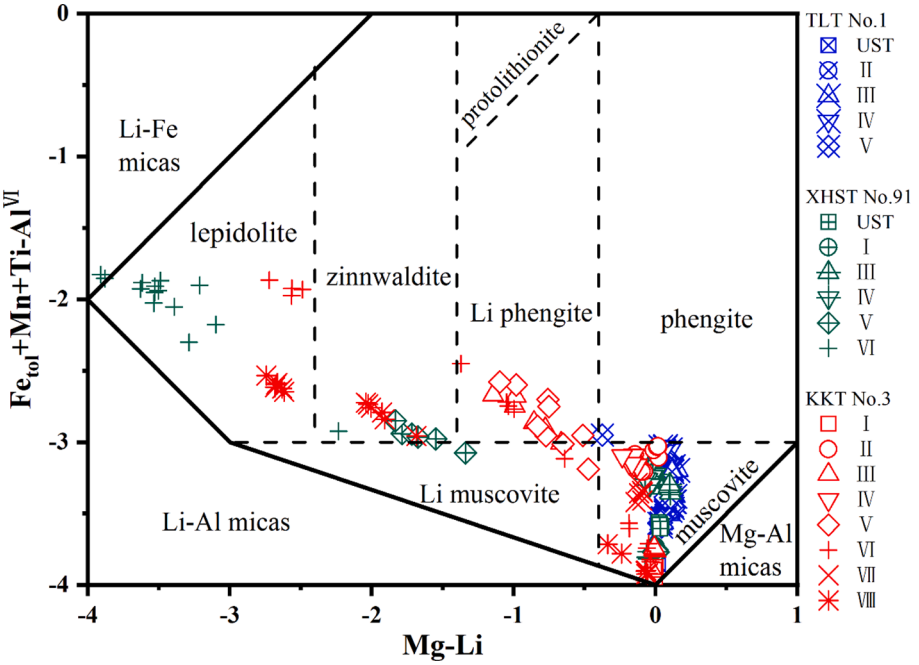

Fig. 4. Plot of Mg-Li versus Fe + Mn + Ti-Al^{VI} for micas from the TLT No.1, XHST No.91 and KKT No.3 pegmatites, after Tischendorf et al. (1997). UST: unidirectional solidification texture (the elongate growth of crystals inward from a contact with host rock).

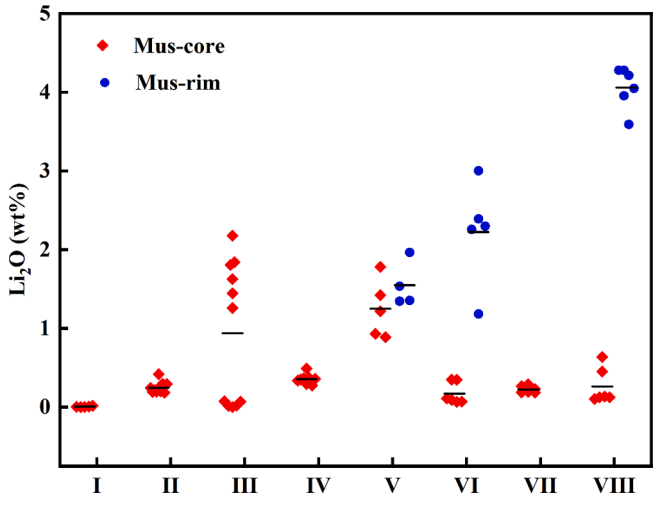

Fig. 5. Li_2O content for muscovite, muscovite-cores and muscovite-rims from different texture zones of the KKT No.3 pegmatite.

calculated, the concentration of Li_2O in montebrasite in both pegmatites is about 10.10 wt%. The concentration of MnO, CaO, Na_2O, and MgO are near or below the detection limits (Table 4).

4.4. Texture and compositional characteristics of holmquistite

Holmquistite is the only rare Li-bearing mineral that has been found in the altered host rocks (biotite–quartz schist) of the TLT No.1 pegmatite (Fig. 2i). Holmquistite occurs as a coarse prism with radial shape, which is blue, green, and purple under cross-polarized light (Fig. 8a). According to its BSE images, massive holmquistite is homogeneous, associated with apatite and ilmenite (Fig. 8b).

Based on the amphibole general formula of $A_{0-1}B_2C_5T_8O_{22}W_2$ calculated (Li et al., 2020) and the concentration of Li_2O from LA-ICPMS data (3.96–4.07 wt%), the concentration of H_2O is about 2.25 wt%. and the concentration of major elements in holmquistite does not significantly change (Table 5). In addition to Li, other rare-metal elements, such as Be (0.45–0.88 ppm), Rb (0.01–0.35 ppm), Cs (0.31–2.00 ppm), Nb (0.01–0.14 ppm), and Ta are near or below the detection limits.

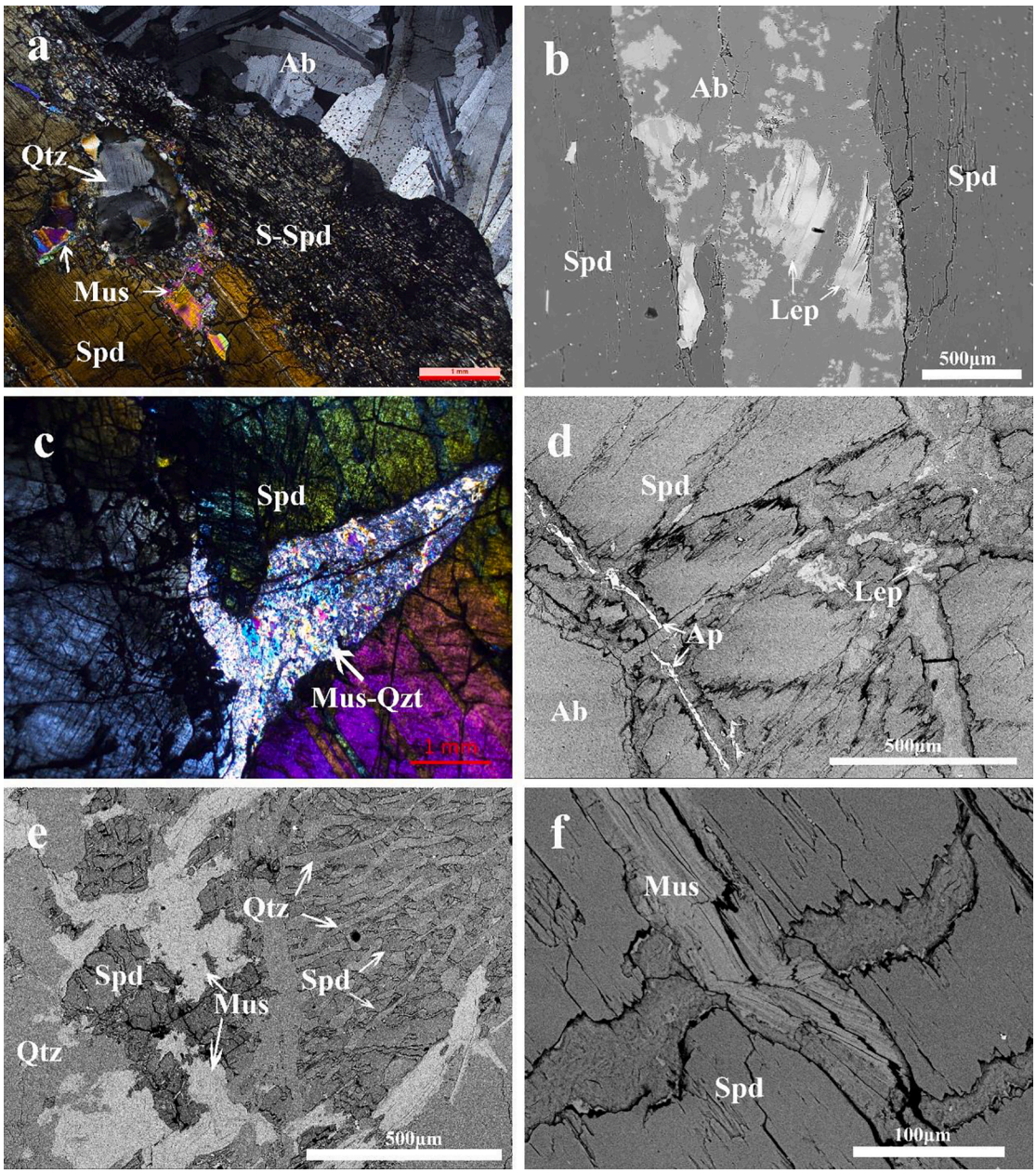

Fig. 6. Photomicrographs and BSE images of spodumene from the KKT No.3 pegmatite (a, b, d), XHST No.91 pegmatite (c) and TLT No.1 pegmatite (e-f). (a) Quartz and muscovite between primary spodumene and secondary fine-grained spodumene. (b) Albite and lepidolite occur in the fracture of spodumene. (c) Cryptocrystalline quartz and muscovite assemblage in the bay of spodumene. (d) Apatite and lepidolite fine veinlets along cleavages in the spodumene. (e) Fine veined quartz cross the spodumene, muscovite occur along the rim of spodumene. (f) Muscovite in the cleavages of spodumene. Mineral abbreviations: Ab = albite; Qtz = quartz; Mus = muscovite; Spd = spodumene; S-Spd = secondary-spodumene; Lep = lepidolite; Ap = apatite.

5. Discussion

5.1. Lithium mineralization during the evolution of the magmatic system

There are many mineral species rich in Li in the studied pegmatites. Spodumene, lepidolite, elbaite, and lithiophilite are found in the KKT No.3 pegmatite, while spodumene, lepidolite, montebrasite, elbaite, and lithiophilite are found in the XHST No.91 pegmatite. Furthermore, spodumene, montebrasite, lithiophilite, and holmquisite are found in the TLT No.1 pegmatite (Table 1, Figs. 2, 7). Generally, spodumene is the most important ore mineral from Li mineralization.

Previous experimental studies estimated the degree of Li enrichment in pegmatite-forming melts at the saturation of Li-aluminosilicate minerals at temperatures relevant to the pegmatite formation (London and Morgan, 2017; Maneta and Baker, 2014; Maneta et al., 2015; Stewart, 1978). Crystallization experiments performed by Maneta and Baker (2014) developed virgilite at 500 MPa and 500 °C, yielding a saturation concentration of approximately 1.27 wt% Li_2O in the coexisting melt. Based on data from Maneta et al. (2015), Li–aluminosilicate saturation occurs with 0.9–1.3 wt% Li_2O in melts. Experiments with the 0.16 wt% Li_2O Macusani obsidian performed by London and Morgan (2017) crystallized petalite when 1.05 wt% Li_2O in melts by the 70 %–80 % fractional crystallization.

These experimental results match quite well the average Li concentrations in natural Li-mineralized pegmatites (Table 6). For the KKT No.3 pegmatite, the average content of Li_2O in the whole rock is 0.35 wt %. The ore content of zones I–IV accounts for about 70 % of the whole rock, indicating that the initial magma containing 0.35 wt% Li_2O can

Table 3
Representative average compositions of spodumene samples from studied pegmatites.

pegmatite	KKT No.3			XHST NO.91		TLT01
Zone	V	VI	VIII	V	VI	V
Analysis	Rang (n = 6)	Rang (n = 6)	Rang (n = 6)	Rang (n = 8)	Rang (n = 8)	Rang (n = 33)
SiO_2	63.38–64.52	64.54–65.31	64.31–64.86	64.36–65.09	63.89–65.25	64.03–65.36
Al_2O_3	26.05–27.04	27.59–28.16	26.87–27.83	27.37–27.96	26.57–27.21	26.61–27.79
FeO	1.06–1.48	0.18–0.20	0.18–0.23	0.35–0.42	0.64–0.89	0.19–0.85
MnO	0.00–0.03	0.00–0.02	0.00–0.01	0.00–0.02	0.00–0.01	0.00–0.03
MgO	0.04–0.10	0.08–0.12	0.08–0.14	0.01–0.03	0.09–0.15	0.02–0.14
CaO	0.00–0.10	0.00–0.01	0.00–0.01	0.00–0.01	0.00–0.01	0.00–0.02
Na_2O	0.14–0.75	0.07–0.16	0.09–0.14	0.08–0.14	0.12–0.18	0.05–0.27
K_2O	0.00–0.03	0.00–0.01	0.00–0.01	0.00–0.01	0.00–0.01	0.00–0.02
Ti_2O	0.00–0.00	0.00–0.00	0.00–0.05	0.00–0.03	0.00–0.01	0.00–0.10
P_2O_5	0.00–0.00	0.00–0.00	0.00–0.00	0.00–0.00	0.00–0.00	0.00–0.01
Cr_2O_3	0.00–0.00	0.00–0.00	0.00–0.01	0.00–0.02	0.00–0.03	0.00–0.04
Li_2O*	7.32–7.92	7.95–8.04	7.89–7.99	7.84–8.03	7.85–7.96	7.69–8.08
Total	99.18–100.88	100.53–101.98	99.65–101.11	100.32–101.19	99.63–101.73	99.84–101.46

(n) in parenthesis: determined points; /: below detection limit; *: the amount of Li_2O was calculated on the basis of stoichiometry.

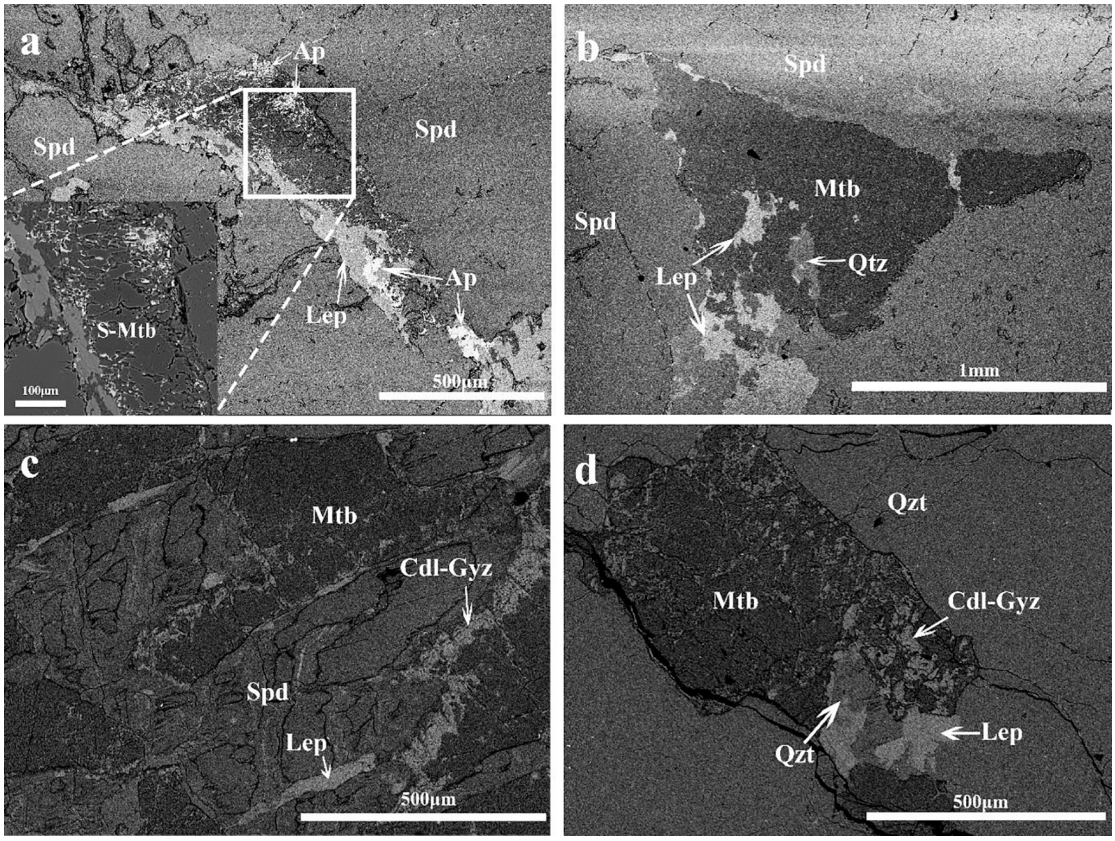

Fig. 7. BSE images of primary montebrasite and its alteration assemblages in the XHST No.91 pegmatite (a-b) and TLT No.1 pegmatite (c-d). (a) Secondary montebrasite occurs as spongy shape and its lepidolite and apatite forming veinlets along cleavages between spodumene. (b) Montebrasite and lepidolite occure with spodumene. (c) Spodumene and montebrasite occur interlacing, accompanied by crandallite-goyazite series and lepidolite. (d) Crandallite-goyazite series and lepidolite locally occured of montebrasite. Abbreviations: Mtb = montebrasite; S-Mtb = secondary-montebrasite; Ap = apatite; Lep = lepidolite; Qtz = quartz; Spd = spodumene; Cdl = crandallite; Gyz = goyazite.

reach Li_2O concentrations of at least 0.95 wt% after 70 % fractional crystallization. With the gradual enrichment of Li in the process of fractional crystallization, a large amount of spodumene began to crystallize in zone V when the content of Li_2O reached up to ~ 1.0 wt%. In addition, the Bailongshan deposit, a recently discovered super-large Li deposit in Xinjiang, China, composed of the 52 ore-bearing pegmatites, hosts about 5.06 million tons Li_2O at 1.58 % (Wang et al., 2021; Yan et al., 2022). A newly discovered super-large pegmatite Li deposit in the Qiongjiagan area of the Higher Himalayan Belt, 59 analyzed samples have average 1.30 wt% Li_2O content (Qin et al., 2021). Stewart (1978) summarized approximately 1.5 wt% Li_2O in pegmatites with spodumene or petalite. Therefore, comparing with the pervious experimental results and natural Li-mineralized pegmatites, Li mineralization occurs with 1.5 ± 0.5 wt% Li_2O in melts, which may experience extreme fractionation crystallization.

Owing to its unique crystal structure and widespread nature in granite–pegmatite systems, micas had been frequently used as an excellent indicator of the evolution degree and the metallogenic mechanism in the pegmatite (Černý, 1982; Černý and Burt, 1984; Li et al., 2021b; Wang et al., 2018; Xing et al., 2020). Since the early work by

Table 4
Representative compositions of the montebrasite from the studied pegmatites.

pegmatite	XHST No.91		TLT No.1
Zone	VI	VI#	V
Analysis	Rang (n = 5)	Rang (n = 5)	Rang (n = 14)
Al_2O_3	35.47–36.71	38.94–40.89	35.03–36.51
FeO	0.04–0.08	0.06–0.08	0.10–0.18
MgO	0.00–0.01	0.00–0.00	0.00–0.01
MnO	0.00–0.02	0.00–0.03	0.00–0.02
CaO	0.00–0.01	0.01–0.11	0.00–0.12
SrO	0.00–0.00	0.00–0.00	0.00–0.03
Na_2O	0.00–0.00	0.00–0.00	0.00–0.02
SO_3	0.00–0.03	0.00–0.02	0.00–0.02
P_2O_5	47.58–48.68	52.03–53.89	47.42–48.81
F	0.96–1.49	0.85–2.65	1.27–2.08
Cl	0.00–0.01	0.00–0.00	0.00–0.01
Li2O*	10.00–10.23		9.92–10.24
H2O*	5.43–5.64		5.18–5.51
O = F	0.40–0.62		0.53–0.87
Total	99.29–102.02	92.44–95.61	99.18–102.11

(n) in parenthesis: determined points; /: below detection limit; *: the amount of Li_2O and H_2O was calculated on the basis of stoichiometry. As the standard chemical formula of the altered secondary montebrasite in the zone VI# is not known, the amount of Li_2O and H_2O cannot be calculated.

Table 5
Representative chemical and trace element compositions of holmquisite from TLT No.1 pegmatite (determined by EMPA and LA-ICP-MS).

Analysis	1	2	3	4	Rang (n = 6)
EPMA (wt%)					
SiO_2	60.36	59.25	59.70	59.38	59.16–60.36
TiO_2	0.01	0.01	/	/	0.00–0.01
Al_2O_3	13.34	13.57	13.43	13.68	13.34–13.68
FeO	10.07	10.05	10.11	10.27	10.05–10.80
MnO	0.22	0.29	0.24	0.26	0.22–0.29
MgO	10.43	10.28	10.66	10.47	10.05–10.66
CaO	/	0.03	/	/	0.00–0.03
Na_2O	0.02	0.18	0.07	0.09	0.02–0.18
K_2O	/	/	/	/	/
F	/	0.09	/	0.01	0.00–0.09
H_2O*	2.29	2.23	2.28	2.27	2.23–2.29
O = F	0.00	0.04	0.00	0.01	
Li_2O	4.07	3.81	3.96	4.08	3.96–4.08
Total	100.81	99.74	100.46	100.52	99.74–100.81
LA-ICP-MS (ppm)					
Be	0.88	0.45	0.85	0.48	0.45–0.88
B	37.28	40.97	46.11	33.18	33.18–46.11
Rb	0.20	0.35	0.16	0.01	0.01–0.35
Cs	1.39	2.00	0.31	0.48	0.31–2.00
Nb	0.04	0.14	0.05	0.01	0.01–0.14
Ta	/	0.01	/	/	0.00–0.01

(n) in parenthesis: determined points; /: below detection limit; *: the amount of H_2O was calculated on the basis of stoichiometry, Li_2O content from LA-ICP-MS analysis.

Černý et al. (1985), the K/Rb and K/Cs ratios of micas have been widely used for monitoring the extent of fractional crystallization of granites and pegmatites (London, 2022). The K/Rb ratios of micas tend to decrease with the increasing content of F from the less-evolved outer zones to the more-evolved inner zones in the studied pegmatites (Fig. 9), reflecting the increasing degree of magma differentiation. The K/Rb ratios of micas amount to approximately 5, indicating a very high degree of differentiation evolution for the studied pegmatites. Moreover the K/Rb ratios of micas from each pegmatite are plotted against Li, Rb, Cs, and Ta (Fig. 9a, e, g, i), indicating that the concentrations of these elements are gradually increasing from the outer to the inner zones in the studied pegmatites. The K/Rb–Be and K/Rb–Nb diagrams show no significant correlation (Fig. 10b, f), implying that Be and Nb are less enriching with the magma differentiation. Additionally, the concentrations of B and Ga in the TLT No.1 pegmatite are generally lower than those in the KKT No.3 pegmatite and in the XHST No.91 pegmatite (Fig. 10c, d). However, Ba is opposite (Fig. 10e), possibly indicating initial melt with distinction derived from different sources.

After spodumene, the amblygonite–montebrasite group minerals are the next important Li-rich phosphates, which commonly occur with apatite in the LCT family of pegmatite (London, 2008). In this study, montebrasite was observed in the XHST No.91 pegmatite and TLT No.1 pegmatite (Fig. 7, Table 4) but not in the KKT No.3 pegmatite, indicating that these minerals have a lower degree of crystallization in the KKT No.3 pegmatite. London et al. (1999) described the petalite–montebrasite equilibrium that produces montebrasite with increasing P_2O_5 concentrations of melt,

$LiAiSi_4O_{10}$ + 0.5P_2O_5 (melt) + 0·.5H_2O (melt) = $LiAlPO_4(OH)$ + 4SiO_2 (crystal or melt),

the equilibrium buffers P content at 1.4 wt% P_2O_5 in melt at 525 °C and 200 Mpa. The occurrence of montebrasite in the XHST No.91 pegmatite and TLT No.1 pegmatite indicates comparable Li concentrations and increasing P_2O_5 concentrations in the melt. However, the absence of montebrasite in the KKT No.3 pegmatite may be attributed to a large amount of apatite crystals in the saccharoidal albite zone (zone II) (Zhang, 2001), which consumes a large concentration of phosphorus in the melt. Moreover, Xu et al. (2019) proposed that the magma immiscibility mechanism of the phosphate melt and silicate melt in the Xiekusite pegmatite is reflected by the inclusions of the montebrasite–lithiophylite association in the rock.

In summary, the KKT No.3 pegmatite, XHST No.91 pegmatite, and TLT No.1 pegmatite have a very high degree of differentiation that gradually evolved from the outer to the inner zones. The magma fractional crystallization played a critical role for Li mineralization.

5.2. The hydrothermal alteration recorded in zoned micas, spodumene, and montebrasite

Depending on the absolute and relative activities of $(PO_4)^{3-}$, F^-, H^+, Na^+, and K^+, the bulk of Li can be incorporated into three mineral assemblages: (i) anhydrous aluminosilicates, (ii) phosphates, and (iii) (Li, F)-enriched micas (Černý et al., 1985). Owing to their instability in hydrothermal fluids, these Li-rich minerals are extensively altered in pegmatites (London and Burt, 1982).

Muscovite appears in zones, with Li, F-rich rim of muscovite commonly presents narrow and discontinuous ring edges at the outer edge of the muscovite mineral particles in the inner zones of the KKT No.3 pegmatite and XHST No.91 pegmatite (Fig. 3a, b, d). The most common irregular boundary probably stems from muscovite dissolution owing to the alteration of late hydrothermal fluids. This type of incomplete and discontinuous rim zone is formed during the interaction between crystals and fluid, which possibly represents the end of magmatism and is related to the action of fluids under the subsolid phase. This evidence was provided by a previous research that investigated how fluid exsolution occurred between zones IV and V in the KKT No.3 pegmatite (Zhang et al., 2008a). Moreover, the exsolved fluids gradually evolved with increasing Li and F concentrations. The alteration effect becomes increasingly intense from zone V to VIII in the KKT No.3 pegmatite, which is recorded in zoned muscovite, such as the concentrations of F and Li_2O in the altered rims of muscovite (2.79 wt% F and 1.53 wt% Li_2O in zone V; 3.73 wt% F and 2.26 wt% Li_2O in zone VI; and 5.98 wt% F and 4.21 wt% Li_2O in zone VIII, respectively). By contrast, the core domains of zoned muscovite have lower concentrations of F and Li_2O from zone V to VIII (2.34 wt% and 1.22 wt% in zone V; 0.91 wt% and 0.34 wt% in zone VI; 0.42 wt% and 0.12 % in zone VIII, respectively) (Table 2, Fig. 5), suggesting that the magmatogenic cores of muscovite have decresing Li and F concentrations in the melt from zone V to VIII after fluid exsolution and spodumene crystallization. Moreover, the exsolved Li and F-rich fluid could have altered the micas in the early structural zone III (Figs. 4, 5), resulting in forming Li-rich phengite. The

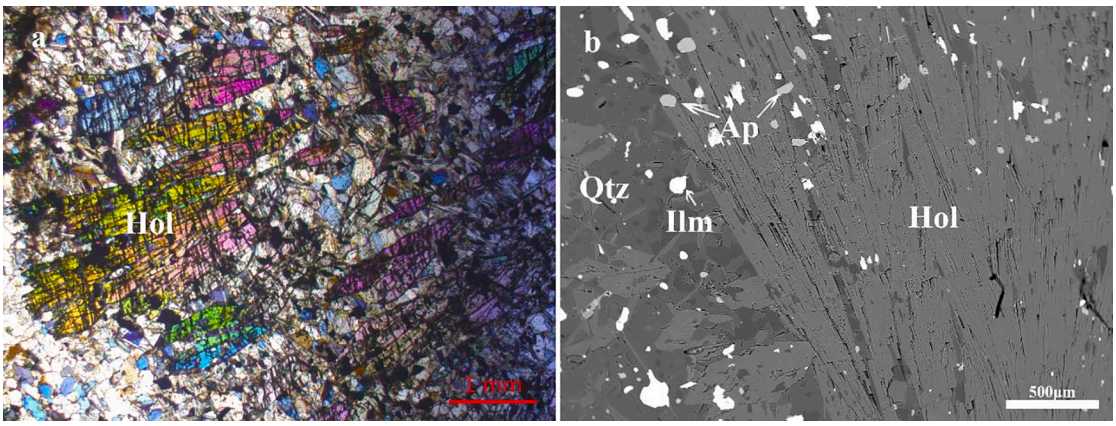

Fig. 8. Photomicrographs and BSE images of holmquisite from the TLT No.1 pegmatite. (a) holmquisite occurs as radial shape in the altered wall rocks. (b) some ilmenite and apatite occur with holmquisite.

Table 6
Grade-tonnage date for Li in the global major to giant Li-bearing pegmatites.

Country	Deposite	Size (Mt)	Li_2O grade (%)	Main mineral	Reference
Australia	Greenbushes	157	2.25	Spodumene	Groves et al. (2022)
	Kathleen Valley	156	1.4	Spodumene	
	Pilgangoora	156	1.25	Spodumene	
	Mount Marion	78	1.37	Spodumene	
	Mount Cattlin	17	1.08	Spodumene	
Cannada	Whabouchi	37	1.16	Spodumene	
	James Bay	40	1.4	Spodumene	
	Tanco	7.3	2.76	Petalite	
	Georgia Lake	11.7	1.14	Spodumene	Breaks et al. (2008)
	Separation Rapids	5.24	1.31	Spodumene	Sweetapple (2000)
China	Jiajika	5	1.4	Spodumene	Fu et al. (2021)
	Bailongshan	5	1.5	Spodumene	Wang et al. (2021)
	Qiongjiagan	1	1.30	Spodumene	Qin et al. (2021)
	Koktokay No.3	0.05	1.38	Spodumene	Zou and Li (2006)
Zimbabwe	Bikita	12	1.4	Spodumene	Bradley et al. (2017)
Mali	Goulamina	44	1.48	Spodumene	Groves et al. (2022)
Portugal	Mina do Barroso	24	1.02	Spodumene	
Russia	Kolmozero	74	1.14	Spodumene	

occurrence of euhedral and secondary subhedral lepidolite in the inner zone of the KKT No.3 pegmatite and XHST No.91 pegmatite (Fig. 3c, 6b, d; Table 2) indicates that the interaction between Li and F-rich melts/fluids occurs in the inner zones. By contrast, the zoned muscovite and lepidolite are not observed in the TLT NO.1 pegmatite. Only some apatite veinlets along the cleavage planes of the euhedral muscovite were observed (Fig. 3e, f, 4), suggesting that the activities of the F-rich fluid are relatively weak compared with those taking place in the KKT No.3 pegmatite and XHST No.91 pegmatite. The high fluid activities of F^- and H^+ led to the precipitation of lepidolite as the Li-rich phase. In the TLT No.1 pegmatite, lepidolite is not observed in the hand specimen and SEM, which demonstrates the smaller F concentration in the TLT No.1 pegmatite.

The metasomatic alteration of spodumene usually occurred along the cleavages, fractures, and borders of the host primary phases. The albitization of spodumene involved Na^+ for Li^+ exchange (Fig. 6b, d), which may be described by the reactions:

$$LiAlSi_2O_6 + SiO_2 + Na^+ = NaAlSi_3O + Li^+.$$

(London and Burt, 1982).

Moreover, spodumene is directly converted to muscovite and released silica in zone V (Fig. 5a, c, e), which is consistent with the following reaction:

$$3LiAlSi_2O_6 + K^+ + 2H^+ = KAl_3Si_3O_{10}(OH)_2 + 3SiO_2 + 3Li^+.$$

(London and Burt, 1982; Yin et al., 2020),

which reflects that the K-rich acidic fluid exists in the late hydrothermal stage. Moreover, the vimineous apatite grains and lepidolite grains occur along the cleavage planes of the spodumene (Fig. 6b, d), which are considered to have grown as a result of the P-rich and F-rich hydrothermal processes. Similarly to the XHST No.91 pegmatite, a portion of spodumene is altered to a bay shape, which fills to form secondary cryptocrystalline muscovite and quartz (Fig. 6c). In the TLT No.1 pegmatite, quartz is filled with veins along the cleavages and fractures of spodumene, and secondary muscovite is grown along the border of the pegmatites (Fig. 6e), which is consistent with the above reaction. Based on the above altered relation of the studied pegmatites, hydrothermal fluids metasomatic alteration and regrowth of spodumene indicate Li reactivated and leached into the hydrothermal fluids in the inner zones, which is bad for the Li mineralization.

London and Burt (1982) suggested that the primary lithium phosphates appear to have crystallized after spodumene in the White Picacho pegmatites, which imply that successive, fluid-saturated magmas became increasingly rich in phosphorus. As from Table 4, the appearance of montebrasite rather than amblygonite illustrates that the melt contained more H_2O than F during the late-stage evolution of the pegmatite. In the XHST No.91 pegmatite and the TLT No.1 pegmatite, spodumene eventually became unstable with respect to montebrasite and quartz (Fig. 7a, c), in accordance with the reaction of previous studies:

$$LiAlSi_2O_6 + PO_2(OH)\ (melt) = LiALPO_4(OH) + 2SiO_2.$$

(London, 2017; London et al., 1999),

which implies that the increased activities of phosphorus as crystallization differentiation proceeded and montebrasite appeared to crystallize after spodumene. Primary assemblages containing amblygonite–montebrasite should require comparable Li concentrations in melt because the silicate–phosphate equilibrium above is mostly a function of the $[P_2O_5]$ activity (London, 2008). Moreover, montebrasite is generally affected by postmagmatic fluids, which can initiate various metasomatic and/or dissolution–crystallization processes and generate different sequences of metasomatic alteration, such as fluorapatite, crandallite, muscovite, and lepidolite (London and Burt, 1982; Rao et al., 2017; Shirose and Uehara, 2014). In the inner zones of the XHST No.91 pegmatite and the TLT No.1 pegmatite, the textural relationships of alteration assemblages, hydroxyl–apatite, and minor

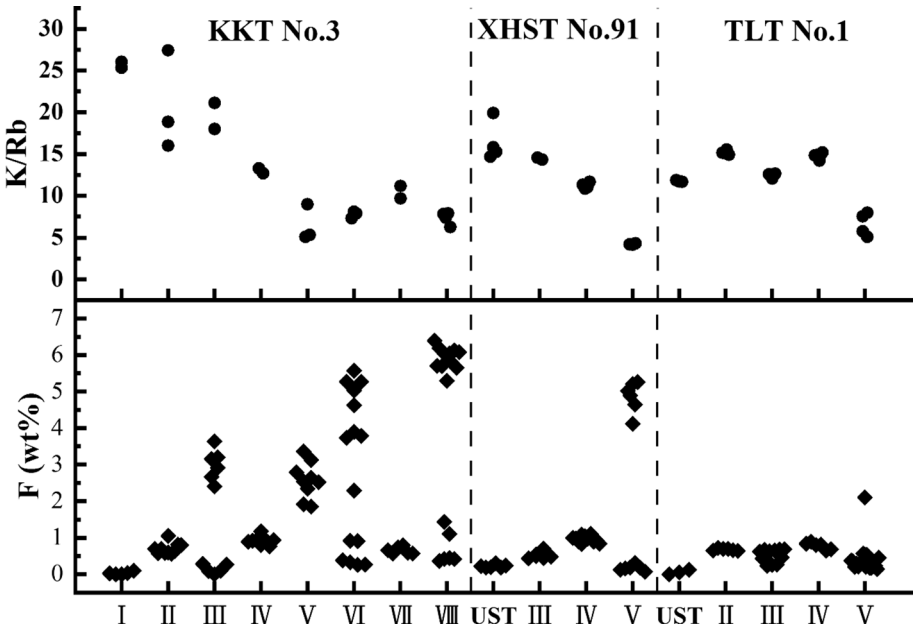

Fig. 9. K/Rb ratios and F content for micas from different texture zones of the KKT No.3, XHST No.91 and TLT No.1 pegmatite.

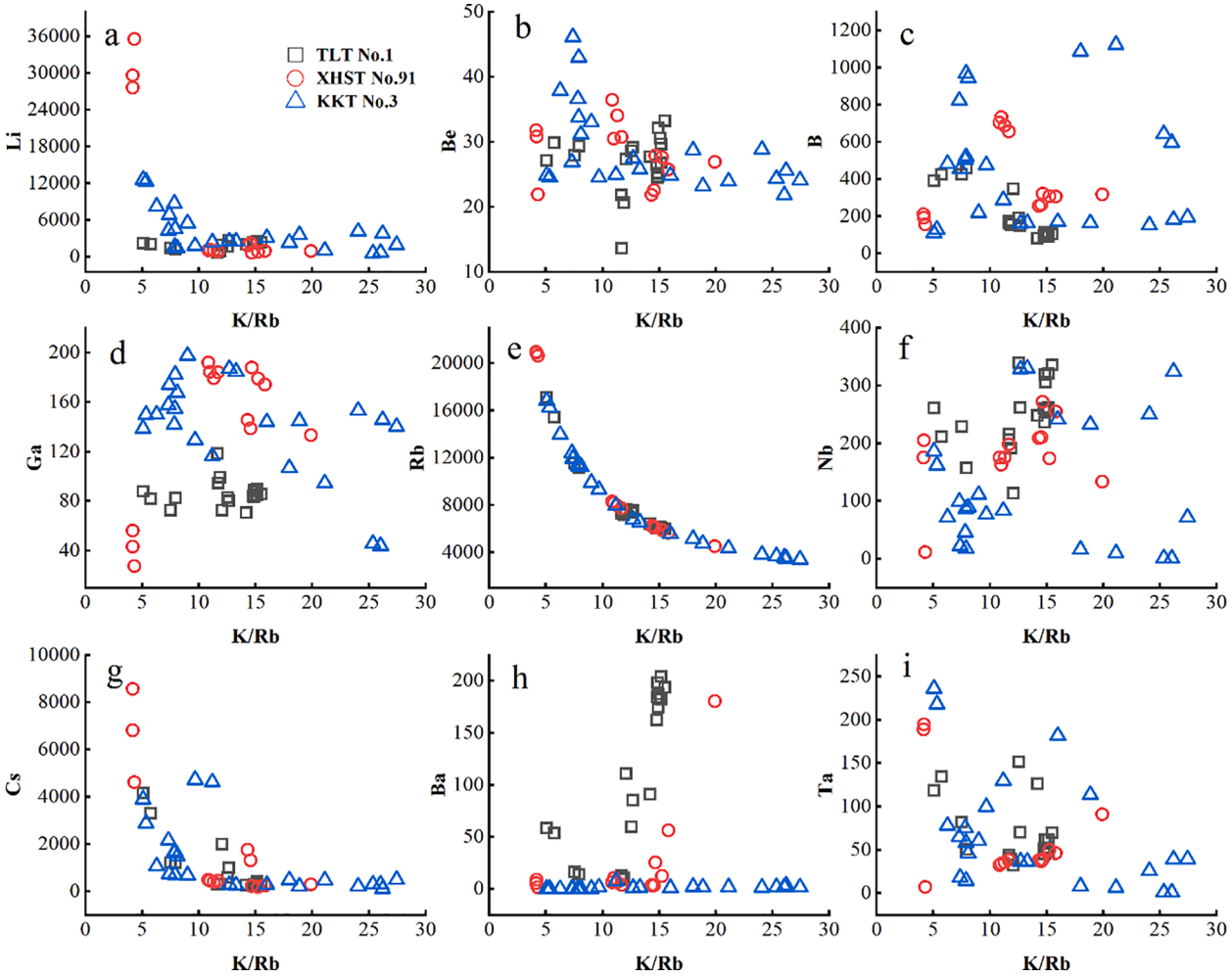

Fig. 10. K/Rb versus Li, Be, B, Ga, Rb, Nb, Cs, Ba and Ta plots in micas from the KKT No.3 pegmatite, XHST No.91 pegmatite and TLT No.1 pegmatite.

crandallite–goyazite series (Fig. 7a, c, d), which indicate the initial cation metasomatism of primary and secondary montebrasite, involved Ca for Li ion exchange due to Ca-rich later hydrothermal fluid. As the leached Li accumulates in the K-rich acidic hydrothermal fluid, some Li-bearing muscovite and lepdolite will be precipitated nearby (Fig. 7a–d). Furthermore, the Li-rich hydrous fluid was diffused to enter the wall rock, and metasomatism occurs with the decrease of temperature and pressure, which explains the large amount of holmquistite found in the TLT No.1 pegmatite that altered the surrounding rock (Fig. 2i, 8a and b; Table 5).

Either altered spodumene or montebrasite causes Li to leach into the hydrothermal fluid and even into the surrounding rock, which obviously destroys Li mineralization. On one hand, the reactivation and migration of Li during the hydrothermal stages of the pegmatites would alter primary muscovite to the rims of Li-bearing muscovite or lepidolite. On the other hand, it could directly reprecipitate and crystallize lepidolite (occurrence of the lepidolite–lamellar albite zone of the KKT No.3 pegmatite and lepidolite veins of the XHST No.91 pegmatite), elbaite (occurring in both the pegmatites), and other rare Li-rich minerals in the inner zones, or migrate outward to the wall rock and occur holmquistite. Thus, these processes indicate reactivation and migration of Li in the hydrothermal stage and would destroy Li mineralization in the magmatic stage.

6. Conclusions

1. The KKT No.3 pegmatite, XHST No.91 pegmatite, and TLT No.1 pegmatite record an early-to-late magmatic–hydrothermal progress from the outer to inner zones and show very high degree of differentiation evolution.
2. Fractional crystallization is the most important factor that controls the Li mineralization in the magmatic stage for the spodumene-bearing pegmatites in the Altai.
3. In the inner zones of the pegmatites, the primary micas, spodumene, and montebrasite were easily altered by the late-stage hydrothermal fluids, which negatively affect Li mineralization. Therefore, the reactivation and migration of Li in the hydrothermal stage would destroy Li mineralization in the pegmatites.

Declaration of Competing Interest

The authors declare that they have no known competing financial interests or personal relationships that could have appeared to influence the work reported in this paper.

Data availability

Data will be made available on request.

Appendix A. Supplementary data

Supplementary data to this article can be found online at https://doi.org/10.1016/j.oregeorev.2022.105058.

References

Bai, Y.X., Shen, P., Cao, C., Pan, H., Li, C., Luo, Y., Feng, H., Suo, Q., 2021. Geochemical characteristics and significance of apatite from the Koktokay pegmatitic rare-metal deposit, Altay, Xinjiang. Acta Petrol. Sin. 37, 2843–2860 in Chinese with English abstract.

BGMRX (Bureau of Geology and Mineral Resources of Xinjiang Uygur Autonomous Region), 1993. Regional geology of Xinjiang Uygur Autonomous Region. People's Republic of China, Ministry of Geology and Mineral Resources. Geological Memoirs, Series, vol. 1, No. 32. Geological Publishing House, Beijing, pp. 6–206 (in Chinese).

Bradley, D.C., McCauley, A.D., Stillings, L.L., 2017. Mineral-Deposit Model for Lithium-Cesium-Tantalum Pegmatites. U.S. Geological Survey, Reston.

Breaks, F.W., Selway, J.B., Tindle, A.G., 2008. The Georgia Lake rare-element pegmatite field and related S-type, peraluminous granites, Quetico Subprovince, north-central Ontario: Ontario Geological Survey, Open File Report 6199.

Cai, K.D., Sun, M., Yuan, C., Zhao, G.C., Xiao, W.J., Long, X.P., Wu, F.Y., 2010. Geochronological and geochemical study of mafic dykes from the northwest Chinese Altai: Implications for petrogenesis and tectonic evolution. Gondwana Res. 18, 638–652.

Cai, K., Sun, M., Yuan, C., Zhao, G., Xiao, W., Long, X., Wu, F., 2011a. Prolonged magmatism, juvenile nature and tectonic evolution of the Chinese Altai, NW China: Evidence from zircon U-Pb and Hf isotopic study of Paleozoic granitoids. J. Asian Earth Sci. 42, 949–968.

Cai, K.D., Sun, M., Yuan, C., Long, X.P., Xiao, W.J., 2011b. Geological framework and Paleozoic tectonic history of the Chinese Altai, NW China: a review. Russ. Geol. Geophys. 52, 1619–1633.

Cai, K.D., Sun, M., Yuan, C., Zhao, G.C., Xiao, W.J., Long, X.P., Wu, F.Y., 2011c. Geochronology, petrogenesis and tectonic significance of peraluminous granites from the Chinese Altai, NW China. Lithos 127, 261–281.

Cai, K.D., Sun, M., Yuan, C., Xiao, W.J., Zhao, G.C., Long, X.P., Wu, F.Y., 2012. Carboniferous mantle-derived felsic intrusion in the Chinese Altai, NW China: Implications for geodynamic change of the accretionary orogenic belt. Gondwana Res. 22, 681–698.

Černý, P., 1982. Petrogenesis of granitic pegmatites. In granitic pegmatites in science and industry, Mineral.assoc.canada Short Course, p. 8.

Černý, P., Burt, D.M., 1984. Paragenesis, crystallochemical characteristics, and geochemical evolution of micas in granite pegmatites. In: Bailey, S.W. (Ed.), Micas. Reviews in Mineralogy, Mineralogical Society of America, Chantilly,Virginia. 13, 257-297.

Černý, P., Meintzer, R.E., Anderson, A.J., 1985. Extreme fractionation in rare-element granitic pegmatites – Selected examples of data and mechanisms. Can. Mineral. 23, 381–421.

Che, X.D., Wu, F.Y., Wang, R.C., Gerdes, A., Ji, W.Q., Zhao, Z.H., Yang, J.H., Zhu, Z.Y., 2015. In situ U-Pb isotopic dating of columbite–tantalite by LA–ICP–MS. Ore Geol. Rev. 65, 979–989.

Chen, J.F., 2011. Geochemistry of the plate part in Altai No. 3 PegmAtite And Its formAtion And Evolution: A DissertAtion Submitted to GrAduAte University of Chinese AcAdemy of Sciences for the Degree of MAster of Philosophy.

Fu, X.F., Liang, B., Zou, F.G., Hao, X.F., Hou, L.W., 2021. Discussion on metallogenic geological characteristics and genesis of rare polymetallic ore fields in western Sichuan. Acta Geol. Sin. 95, 3054–3068.

Groves, D.I., Zhang, L., Groves, I.M., Sener, A.K., 2022. Spodumene: The key lithium mineral in giant lithium-cesium-tantalum pegmatites. Acta Petrol. Sin. 38, 1–8.

Hulsbosch, N., Hertogen, J., Dewaele, S., Andre, L., Muchez, P., 2014. Alkali metal and rare earth element evolution of rock-forming minerals from the Gatumba area pegmatites (Rwanda): quantitative assessment of crystal-melt fractionation in the regional zonation of pegmatite groups. Geochim. Cosmochim. Acta. 132, 349–374.

Jiang, Y., Sun, M., Zhao, G., Yuan, C., Xiao, W., Xia, X., Long, X., Wu, F., 2011. The 390 Ma high-T metamorphic event in the Chinese Altai: A consequence of ridge-subduction? Am. J. Sci. 310, 1421–1452.

Kaeter, D., Barros, R., Menuge, J.F., Chew, D.M., 2018. The magmatic–hydrothermal transition in rare-element pegmatites from southeast Ireland: LA-ICP-MS chemical mapping of muscovite and columbite–tantalite. Geochim. Cosmochim. Acta. 240, 98–130.

Li, J., Huang, X.L., Fu, Q., Li, W.X., 2021a. Tungsten mineralization during the evolution of a magmatic-hydrothermal system: mineralogical evidence from the Xihuashan rare-metal granite in South China. Am. Mineral. 106, 443–460.

Li, P., Li, J.K., Chen, Z.Y., Liu, X., Huang, Z., Zhou, F.C., 2021b. Compositional evolution of the muscovite of Renli pegmatite-type rare-metal deposit, northeast Hunan, China: implications for its petrogenesis and mineralization potential. Ore Geol. Rev. 138, 104380.

Li, X.Y., Zhang, C., Behrens, H., Holtz, F., 2020. Calculating amphibole formula from electron microprobe analysis data using a machine learning method based on principal components regression. Lithos 362, 105469.

Lichtervelde, M.V., Grégoire, M., Linnen, R.L., Béziat, D., Salvi, S., 2008. Trace element geochemistry by laser ablation ICP-MS of micas associated with Ta mineralization in the Tanco pegmatite, Manitoba, Canada. Contrib. Mineral. Petrol. 155, 791–806.

Linnen, R.L., Cuney, M. Granite-related rare-element deposits and experimental constraints on Ta-Nb-W-Sn-Zr-Hf mineralization, in Linnen R.L. and Samson I.M., eds., rare-element geochemistry and mineral deposits. 2005.

Liu, Y.S., Hu, Z.C., Gao, S., Gunther, D., Xu, J., Gao, C.G., Chen, H.H., 2008. In situ analysis of major and trace elements of anhydrous minerals by LA-ICP-MS without applying an internal standard. Chem. Geol. 257, 34–43.

Liu, C., Wang, R.C., Wu, F.Y., Xie, L., Liu, X.C., Li, X.K., Yang, L., Li, X.J., 2020. Spodumene pegmatites from the Pusila pluton in the higher Himalaya, South Tibet: lithium mineralization in a highly fractionated leucogranite batholith. Lithos 358, 105421.

Liu, C.Q., Zhang, H., 2005. The lanthanide tetrad effect in apatite from the Altay No. 3 pegmatite, Xingjiang, China: an intrinsic feature of the pegmatite magma. Chem. Geol. 214, 61–77.

Liu, F., Zhang, Z.X., Li, Q., Zhang, C., Li, C., 2014. New precise timing constraint for the Keketuohai No. 3 pegmatite in Xinjiang, China, and identification of its parental pluton. Ore Geol. Rev. 56, 209–219.

London, D., 2017. Reading pegmatites: Part 3—what lithium minerals say. Rocks Miner. 92, 144–157.

London, D., 2018. Ore-forming processes within granitic pegmatites. Ore Geol. Rev. 101, 349–383.

London, D., 2022. A Rayleigh model of cesium fractionation in granite-pegmatite systems. Am. Mineral. 107, 82–91.

London, D., Burt, D.M., 1982. Alteration of spodumene, montebrasite and lithiophilite in pegmatites of the white picacho district, Arizona. Am. Mineral. 67, 97–113.

London, D., Morgan, G.B., 2017. Experimental Crystallization of the Macusani Obsidian, with Applications to Lithium-rich Granitic Pegmatites. J. Petrol. 58, 1005–1030.
London, D., Wolf, M.B., Morgan, G.B., Garrido, M.G., 1999. Experimental silicate-phosphate equilibria in peraluminous granitic magmas, with a case study of the Alburquerque batholith at Tres Arroyos, Badajoz, Spain. J. Petrol. 40, 215–240.
London, D., 2008. Pegmatites. Can. Mineral. Special Publication 10, 1–347.
Long, X.P., Sun, M., Yuan, C., Xiao, W.J., Cai, K., 2008. Early Paleozoic sedimentary record of the Chinese Altai: Implications for its tectonic evolution. Sediment. Geol. 208, 88–100.
Lv, Z.H., Zhang, H., Tang, Y., Liu, Y.L., Zhang, X., 2018. Petrogenesis of syn-orogenic rare metal pegmatites in the Chinese Altai: evidences from geology, mineralogy, zircon U-Pb age and Hf isotope. Ore Geol. Rev. 95, 161–181.
Maneta, V., Baker, D.R., 2014. Exploring the effect of lithium on pegmatitic textures: an experimental study. Am. Mineral. 99, 1383–1403.
Maneta, V., Baker, D.R., Minarik, W., 2015. Evidence for lithium-aluminosilicate supersaturation of pegmatite-forming melts. Contrib. Mineral. Petrol. 170.
Messing, E.M., Young, T.B., Hunt, V.B., Roecker, E.B., Vaillancourt, A.M., Hisgen, W.J., Greenberg, E.B., Kuglitsch, M.E., Wegenke, J.D., 1992. Home screening for hematuria: results of a multiclinic study. J. Urol. 148, 289–292.
Qin, K.Z., Zhao, J.X., He, C.T., Shi, R.Z., 2021. Discovery of the Qongjiagang giant lithium pegmatite deposit in Himalaya, Tibet, China. Acta Petrol. Sin. 37, 3277–3286 in Chinese with English abstract.
Rao, C., Wang, R.C., Yang, Y.Q., Hatert, F., Xia, Q.K., Yue, X.G., Wang, W.M.Y., 2017. Insights into post-magmatic metasomatism and Li circulation in granitic systems from phosphate minerals of the Nanping No. 31 pegmatite (SE China). Ore Geol. Rev. 91, 864–876.
Ren, B.Q., Zhang, H., Tang, Y., Lv, Z.H., 2011. LA-ICPMS U-Pb zircon geochronology of the Altai pegmatites and its geological significance. Acta. Mineral. Sin. 31, 587–596.
Roda, E., Keller, P., Pesquera, A., Fontan, F., 2007. Micas of the muscovite–lepidolite series from Karibib pegmatites, Namibia. Mineral. Mag. 71, 41–62.
Shearer, C.K., Papike, J.J., Jolliff, B.L., 1992. Petrogenetic links among granites and pegmatites in the harney peak rare-element granite pegmatite system, black-hills, South-Dakota. Can. Mineral. 30, 785–809.
Shirose, Y., Uehara, S., 2014. Secondary phosphates in montebrasite and amblygonite from Nagatare, Fukuoka Prefecture, Japan. J. Mineral. Petrol. Sci. 109, 103–108.
Sovacool, B.K., Ali, S.H., Bazilian, M., Radley, B., Nemery, B., Okatz, J., Mulvaney, D., 2020. Sustainable minerals and metals for a low-carbon future. Science. 367, 30–33.
Stewart, D.B., 1978. Petrogenesis of lithium-rich pegmatites. Am. Mineral. 63, 970–980.
Sun, M., Long, X.P., Cai, K.D., Jiang, Y.D., Wang, B.Y., Yuan, C., Zhao, G.C., Xiao, W.J., Wu, F.Y., 2009. Early Paleozoic ridge subduction in the Chinese Altai: insight from the abrupt change in zircon Hf isotopic compositions. Sci. China Ser. D-Earth Sci. 52, 1345–1358.
Sweetapple, M.T., 2000. Characteristics of Sn-Ta-Be-Li industrial mineral deposits of the Archaean Pilbara Craton, Western Australia. Australian Geological Survey Organization, Record 2000/44.
Tang, H., Zhang, H., 2018. Characteristics of trace elements in quartz from No.3 Pegmatite, Koktokay area, Xinjiang Autonomous Region, China and implication for magmatic-hydrothermal evolution. Acta Mineral. Sin. 30.
Thomas, R., Davidson, P., 2016. Revisiting complete miscibility between silicate melts and hydrous fluids, and the extreme enrichment of some elements in the supercritical state — Consequences for the formation of pegmatites and ore deposits. Ore Geol. Rev. 72, 1088–1101.
Thomas, R., Davidson, P., Appel, K., 2019. The enhanced element enrichment in the supercritical states of granite–pegmatite systems. Acta Geochim. 38, 335–349.
Tian, R., Zhang, H., Lv, Z., Tang, Y., 2021. Mineralogical characteristics and geological significance of mica in Xiaohusite No. 91 pegmatite in Koktokay mining area, Xinjiang. Acta. Mineral. Sin. 41 in Chinese with English abstract.
Tindle, A.G., Webb, P.C., 1990. Estimation of lithium contents in trioctahedral micas using microprobe data: application to micas from granitic rocks. Eur. J . Mineral. 595–610.
Tischendorf, G., Gottesmann, B., Forster, H.J., Trumbull, R.B., 1997. On Li-bearing micas: estimating Li from electron microprobe analyses and an improved diagram for graphical representation. Mineral. Mag. 61, 809–834.
Veksler, I.V., Thomas, R., 2002. An experimental study of B-, P- and F-rich synthetic granite pegmatite at 0.1 and 0.2 GPa. Contrib. Mineral. Petrol. 143, 673–683.
Wang, R.C., Che, X.D., Zhang, W.L., Zhang, A.C., Zhang, H., 2009. Geochemical evolution and late re-equilibration of Na–Cs-rich beryl from the Koktokay #3 pegmatite (Altai, NW China). Eur. J. Mineral. 21, 795–809.
Wang, T., Tong, Y., Jahn, B.-M., Zou, T.-R., Wang, Y.-B., Hong, D.-W., Han, B.-F., 2007. SHRIMP U-Pb Zircon geochronology of the Altai No. 3 Pegmatite, NW China, and its implications for the origin and tectonic setting of the pegmatite. Ore Geol. Rev. 32, 325–336.
Wang, R., Xie, L., Zhu, Z., Hu, H., 2018. Micas: important indicators of granite-pegmatite-related rare-metal mineralization. Acta Petrol. Sin. 35, 69–75.
Wang, H., Xu, Y.G., Yan, Q.H., Zhan, X.Y., 2021. Research progress on Bailongshang pegmatite type lithium deposit, Xinjiang. Acta Geol. Sin. 95, 3085–3098.
Webster, J.D., Thomas, R., Rhede, D., Forster, H.J., Seltmann, R., 1997. Melt inclusions in quartz from an evolved peraluminous pegmatite: Geochemical evidence for strong tin enrichment in fluorine-rich and phosphorus-rich residual liquids. Geochim. Cosmochim. Acta 61, 2589–2604.
Windley, B.F., Kroner, A., Guo, J.H., Qu, G.S., Li, Y.Y., Zhang, C., 2002. Neoproterozoic to paleozoic geology of the Altai orogen, NW China: new zircon age data and tectonic evolution. J. Geol. 110, 719–737.
Wu, F.Y., Liu, X.C., Ji, W.Q., Wang, J.M., Yang, L., 2017. Highly fractionated granites: Recognition and research. Sci. China-Earth Sci. 60, 1201–1219.
Wu, S., Zhao, J., Zhang, X., Zhang, H., 2015. Magmatic-hydrothermal evolution of the koktokay No.3 Pegmatite, Altay, NW China: evidence from compositional variation of tourmaline. Acta Mineral. Sin. 35, 299–308.
Wu, B., Zou, T., 1989. The genesis of granitic pegmatites in Xinjiang Altai. Miner. Geol. Xinjiang 60–70 in Chinese.
Xing, C.M., Wang, C.Y., Wang, H., 2020. Magmatic-hydrothermal processes recorded by muscovite andcolumbite-group minerals from the Bailongshan rare-element pegmatites in the West Kunlun-Karakorum orogenic belt, NW China. Lithos 364–365, 105507.
Xu, Y., Lu, H., Rao, C., 2019. Mineralogical Behavior of Lithium and Its Implications from the Xiekusite Pegmatite, Altay, Xinjiang. Geol. J. China Univers. 25, 321–332 in Chinese with English abstract.
Xu, Z.Q., Zhu, W.B., Zheng, B.H., Shu, L.S., Li, G.W., Che, X.D., Qin, Y.L., 2021. New energy strategy for lithium resource and the continental dynamics research——celebrating the centenary of the School of Earth Sciences and Engineering, Nanjing University. Acta Geol. Sin. 95, 2937–2954 in Chinese with English abstract.
Yan, Q.H., Wang, H., Chi, G.X., Wang, Q., Hu, H., Zhou, K.L., Zhang, X.Y., 2022. Recognition of a 600-km-long Late Triassic rare-metal (Li–Rb–Be–Nb–Ta) pegmatite belt in the Western Kunlun orogenic belt, western China. Econ. Geol. 117, 213–236.
Yin, R., Huang, X.-L., Xu, Y.-G., Wang, R.-C., Wang, H., Yuan, C., Ma, Q., Sun, X.-M., Chen, L.-L., 2020. Mineralogical constraints on the magmatic–hydrothermal evolution of rare-elements deposits in the Bailongshan granitic pegmatites, Xinjiang, NW China. Lithos 352–353, 105208.
Yuan, C., Sun, M., Xiao, W., Li, X., Chen, H., Lin, S., Xia, X.P., Long, X., 2007. Accretionary orogenesis of the Chinese Altai: insights from Paleozoic granitoids. Chem. Geol. 242, 22–39.
Zhang, H., 2001. The geochemical behaviors and mechanisms of incompatible trace elements in the magmatic-hydrothermal transition system: a case study of Altay No. 3 pegmatite, Xinjiang. The Doctoral Dissertation of Institute of Geochemistry, Chinese Academy of Sciences (in Chinese with English abstract).
Zhang, A.C., Wang, R.C., Hu, H., Chen, X.M., Zhang, H., 2004a. Occurrences of foitite and rossmanite from the Koktokay no. 3 granitic pegmatite dyke, Altai, northwestern China: a record of hydrothermal fluids. Can. Mineral. 42, 873–882.
Zhang, A.C., Wang, R.C., Hu, H., Zhang, H., Zhu, J.C., Chen, X.M., 2004b. Chemical evolution of Nb-Ta oxides and zircon from the Koktokay No. 3 granitic pegmatite, Altai, northwestern China. Mineral. Mag. 68, 739–756.
Zhang, A.C., Wang, R.C., Jiang, S.Y., Hu, H., Zhang, H., 2008a. Chemical and textural features of tourmaline from the spodumene-subtype Koktokay No. 3 pegmatite, Altai, northwestern China: a record of magmatic to hydrothermal evolution. Can. Mineral. 46, 41–58.
Zhang, A.C., Wang, R.C., Li, Y.L., Hu, H., Lu, X.C., Ji, J.F., Zhang, H., 2008b. Tourmalines from the Koktokay No.3 pegmatite, Altai, NW China: spectroscopic characterization and relationships with the pegmatite evolution. Eur. J. Mineral. 20, 143–154.
Zhou, Q.F., Qin, K.Z., Tang, D.M., Ding, J.G., Guo, Z.L., 2013. Mineralogy and significance of micas and feldspars from the Koktokay No. 3 pegmatitic rare-element deposit, Altai. Acta Petrol. Sin. 29, 3004–3022.
Zhou, Q., Qin, K., Tang, D., Wang, C., Tian, Y., Sakyi, P.A., 2015. Mineralogy of the Koktokay No. 3 pegmatite, Altai, NW China: implications for evolution and melt–fluid processes of rare-metal pegmatites. Eur. J. Mineral. 27, 433–457.
Zhu, J.C., Wu, C.N., Liu, C.S., Li, F.C., Huang, X.L., Zhou, D.S., 2000. Magmatic-hydrothermal evolution and genesis of the Altai No. 3 rare metal pegmatite dyke, Altai, China. Geol. J. China Univ. 6, 40–52 in Chinese with English abstract.
Zou, T.R., Li, Q.C., 2006. Rare and Rare Earth Metallic Deposits in Xinjiang, China. Beijing: Geological Publishing House 1–284 (in Chinese with English abstract).